Stochastic Liouville equation simulation of multidimensional vibrational line shapes of trialanine

Thomas la Cour Jansen, Wei Zhuang, and Shaul Mukamel
Department of Chemistry, University of California, Irvine, California 92697-2025

(Received 26 July 2004; accepted 25 August 2004)

The line shapes detected in coherent femtosecond vibrational spectroscopies contain direct signatures of peptide conformational fluctuations through their effect on vibrational frequencies and intermode couplings. These effects are simulated in trialanine using a Green's function solution of a stochastic Liouville equation constructed for four collective bath coordinates (two Ramachandran angles affecting the mode couplings and two diagonal energies). We find that fluctuations of the Ramachandran angles which hardly affect the linear absorption can be effectively probed by two-dimensional spectra. The signal generated at $\mathbf{k}_1+\mathbf{k}_2-\mathbf{k}_3$ is particularly sensitive to such fluctuations. © *2004 American Institute of Physics.* [DOI: 10.1063/1.1807824]

I. INTRODUCTION

The biological activity of proteins is determined by their three-dimensional structure and dynamics.[1] Experimental techniques including nuclear magnetic resonance (NMR),[2–4] linear optical and Raman fluorescence,[5,6] small angel x-ray scattering,[7,8] and Laue diffraction[9,10] are widely used to investigate proteins structures with nanosecond time resolution. While various structural motifs may be distinguished by changes in linear infrared absorption,[11–15] femtosecond multidimensional coherent vibrational spectroscopies facilitate the extraction of more detailed information.[16,17] These techniques are analogous to two-dimensional (2D) NMR[18,19] in that the spectral resolution is enhanced by spreading the signal into multiple dimensions.

Proteins consist of amino acid units connected by amide bonds (Fig. 1). The carbonyl stretch gives rise to the strong amide I infrared absorption ($\sim 1650\ \mathrm{cm}^{-1}$). The 2D IR spectra of the amide I region of many small (<6 units) peptides[20–30] were studied in addition to a handful of investigations for larger systems.[31–34] Extensive experimental[25,26,32] and theoretical[28] work was carried out on the small peptide trialanine (Fig. 1), which contains two amide groups and a terminal carboxylic acid group. The $1725\ \mathrm{cm}^{-1}$ CO stretch of the terminal acid group is spectrally isolated from the $1650\ \mathrm{cm}^{-1}$ and $1670\ \mathrm{cm}^{-1}$ amide CO stretches. The relative orientation of the two coupled amide I modes is thus determined by a single set of Ramachandran angles, making this system ideal for studying the effect of conformational fluctuations on the infrared spectra of peptides.

The interpretation of spectra involves connecting the observable peak positions and line shapes to molecular structure and dynamics. The energies are in general fluctuating with the molecule's instantaneous environment. The peak positions depend on the average environment whereas the spectral line shapes are sensitive both to the static distributions of local environments and their dynamics.

The infrared spectra of the amide I band may be described by the fluctuating exciton Hamiltonian,[35,36]

$$H(t)=H_0(t)+H_{int}(t), \tag{1}$$

where

$$H_0(t)=\sum_i \omega_i(t)B_i^\dagger B_i-\frac{1}{2}\sum_i K_i(t)B_i^\dagger B_i^\dagger B_i B_i + \sum_{j\neq i} J_{ij}(t)B_i^\dagger B_j \tag{2}$$

is the molecular Hamiltonian and

$$H_{int}(t)=\sum_i \mu_i(B_i^\dagger+B_i)E(t) \tag{3}$$

is the interaction with an external electric field $E(t)$. $B_i^\dagger$ and B_i are creation and annihilation operators for the local Harmonic basis of amide I vibrations with frequency ω_i and quartic anharmonicity K_i satisfying the Boson commutator relation $[B_i^\dagger,B_j]=\delta_{ij}$. J_{ij} are intermode couplings and μ_i is the transition dipole.

The fluctuations of all parameters (ω_i, K_i, and J_{ij}) result from large amplitude motions of various conformations as well as coupling to solvent and intramolecular low frequency modes. If the fluctuations are very slow, the dynamics does not affect the line shapes and the simulation simply involves a static averaging over configurations using the instantaneous eigenstates. The line shapes in this limit are denoted inhomogeneous. As long as the fluctuations are not too fast, so that these eigenstates are well separated compared to the nonadiabatic coupling parameter (defined in Sec. II), it is possible to represent the necessary dipole correlation functions as sums over the various excited states, involving one state at a time [see Eqs. (8) and (9)]. If further the energy fluctuations are Gaussian, one can derive closed expressions using the second-order cumulant. This cumulant expansion of Gaussian fluctuations (CGF) (Ref. 37) was reviewed recently.[35]

For faster fluctuations the nonadiabatic parameter is no longer negligible, the direct simulation involves multiple level crossings (see Appendix D) and becomes much more

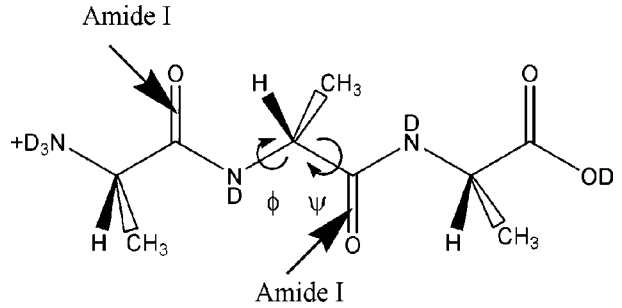

FIG. 1. Trialanine with the Ramachandran angles and amide I modes indicated.

expensive. In this case an alternative approach will be to include explicitly the relevant collective bath modes and to work in an extended phase space, where we consider the evolution of distributions rather than individual trajectories. This is the basis of the Stochastic Liouville equation (SLE) developed by Kubo[38,39] to describe the dynamics of a quantum system perturbed by a stochastic process described by a Markovian master equation. It is widely used in the simulation of electron spin resonance (ESR),[40,41] NMR,[42] and infrared[43,44] line shapes. ESR spectra depend on the orientational motions and the SLE can, for example, be used to account for the effect of rotational diffusion.[40,41] The SLE is used for the description of chemical exchange in NMR,[42,45] where the system can be found in one of several states with different resonance frequencies. Population transfer between states can, for example, be described by the two state jump model[42,46] or reorientational diffusion models.[42,47] Motional narrowing in infrared absorption was studied with the Redfield approach[48] in alkanes with torsional motion[43] and a carbon monooxide iron complex with carbon monooxide exchange.[44] The SLE has also been applied to optical stark spectroscopy,[49,50] where the bath was treated using a Brownian oscillator model. A microscopic derivation of the SLE for excitons was given in Ref. 50.

In this paper we construct a SLE for the amide I band of trialanine. Our model consist of two coupled modes using the Hamiltonian given in Eq. (1). The stochastic processes perturbing the frequencies are described by a Brownian oscillator model. The coupling depends on dihedral angles whose dynamics is also described by Brownian oscillators. Thus the model provides a direct connection between dynamics of the molecular structure fluctuations and the spectrum. The SLE is solved numerically by expansion in the eigenbasis of the relaxation operator. Green's function matrices are computed in the frequency domain using a matrix continued fraction representation.[51]

The time evolution in the adiabatic basis is described in Sec. II. The Liouville equation for the vibrational coordinates is presented in Sec. III. The model for the time evolution of the stochastic collective coordinates giving the structural fluctuations is described in Sec. IV. The SLE for the joint distribution of the vibrational and the stochastic collective coordinates are discussed in Sec. IV. The line shape simulations are carried out in Secs. V and VI. The results are discussed in Sec. VII.

II. ADIABATIC SIMULATIONS OF LINE SHAPES

The time dependent wave function $\phi(t)$ of a quantum system described by the Hamiltonian $H(t)$ satisfies the Schrödinger equation,

$$\frac{d|\phi(t)\rangle}{dt} = -\frac{i}{\hbar} H(t)|\phi(t)\rangle. \tag{4}$$

The instantaneous eigenfunctions $\tilde{\psi}_i(t)$ of $H(t)$ with eigenvalues $\epsilon_i(t)$ constitute a natural orthonormal set known as the adiabatic basis:

$$H(t)|\tilde{\psi}_i(t) = \epsilon_i(t)|\tilde{\psi}_i(t)\rangle. \tag{5}$$

It should be emphasized that the time arguments $\tilde{\psi}_i(t)$ merely denote a *parametric* dependence of the eigenfunctions on time. These functions are not solutions to the time dependent Schrödinger equation. Expanding the time dependent wave function $\phi(t)$ in this basis,

$$\phi(t) = \sum_i c_i(t)\tilde{\psi}_i(t), \tag{6}$$

the time evolution of the expansion coefficients $c_j(t)$ is given by (see Appendix D)

$$\dot{c}_j(t) = -\frac{i}{\hbar}\epsilon_j(t)c_j(t) - \sum_k S_{jk}(t)c_k(t). \tag{7}$$

Here a dot denotes the time derivative and $S_{jk}(t) \equiv \langle \tilde{\psi}_j(t)|\dot{\tilde{\psi}}_k(t)\rangle$ are the nonadiabatic couplings.

The linear optical response is related to the two time correlation function of the dipole operator $\mu(t)$.[52] In the adiabatic approximation where the nonadiabatic couplings S_{jk} in Eq. (7) are neglected, this correlation function is given by

$$\langle \mu(t_2)\mu(t_1)\rangle = \sum_{ab} P(a)\left\langle \mu_{ab}(t_2)\mu_{ba}(t_1) \times \exp\left[-\frac{i}{\hbar}\int_{t_1}^{t_2}\omega_{ba}(\tau)d\tau\right]\right\rangle. \tag{8}$$

Here $\mu_{ab}(t) = \langle \tilde{\psi}_a(t)|\mu|\tilde{\psi}_b(t)\rangle$ is the transition dipole moment between the adiabatic states a and b and $\omega_{ba}(\tau) \equiv \epsilon_b(\tau) - \epsilon_a(\tau)$ is the corresponding frequency. $\langle\cdots\rangle$ denotes the ensemble average.

The third-order response function is similarly given by a sum of four Liouville space pahtways R_i related to the four time correlation function, which in the adiabatic limit is given by (see Appendix D)[52]

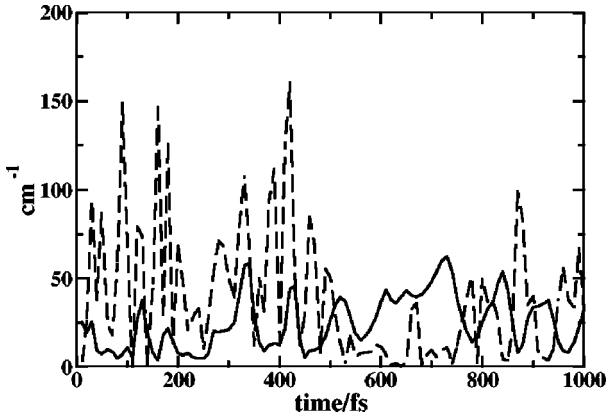

FIG. 2. Solid line—the energy difference between the two amide I eigenstates. Dashed line—the absolute value of the nonadiabatic coupling.

$$\langle \mu(\tau_1)\mu(\tau_2)\mu(\tau_3)\mu(\tau_4)\rangle = \sum_{abcd} P(a)\Big\langle \mu_{ad}(\tau_4)\mu_{dc}(\tau_3)\mu_{cb}(\tau_2)\mu_{ba}(\tau_1) \times \exp\Big(-\frac{i}{\hbar}\int_{\tau_3}^{\tau_4}\omega_{da}(\tau)d\tau - \frac{i}{\hbar}\int_{\tau_2}^{\tau_3}\omega_{ca}(\tau)d\tau - \frac{i}{\hbar}\int_{\tau_2}^{\tau_1}\omega_{ba}(\tau)d\tau\Big)\Big\rangle. \quad (9)$$

Extensive experimental and theoretical work on the interpretation of line shapes of the spectrally isolated OH stretch of HOD (Refs. 53–56) in D_2O and amide I modes of *N*-methyl acetamide (NMA),[57–59] trialanine[25,60–62] and other molecules[63] have been carried out using the adiabatic approximation.

The adiabatic approximation assumes that the adiabatic states obtained by diagonalizing the Hamiltonian at various points along the trajectory retain their identity and no curve crossing occurs. Equations (8) and (9) hold as long as the transitions under consideration are spectrally well separated compared to the nonadiabatic coupling between them so that the adiabaticity parameter $|\hbar S_{jk}/\Delta E_{jk}| \ll 1$, where ΔE_{jk} is the separation between the levels. To test the applicability of this approximation, the nonadiabatic coupling elements and the energy difference between the two eigenstates were calculated for a short trialanine trajectory. Details of the molecular dynamics (MD) simulation are given in Sec. IV. The Hamiltonian [Eq. (1)] was constructed for each point along the trajectory. $J_{12}(t)$ were obtained from the Tasumi map.[64] The frequencies were obtained by adding a constant gas phase value calculated from density-functional theory[65] with a solvent interaction term obtained from the two lowest order derivatives of the solvent-solute interaction potential from the CHARMM27 force field with respect to the CO stretch coordinate.[66] Only the lowest two excited states were considered and $K_i(t)$ was neglected. The eigenvalues and eigenfunctions were obtained by diagonalizing this Hamiltonain at 10 fs intervals and nonadiabatic coupling elements were computed by numerical differentiation. The exciton splitting is compared with the nonadiabatic coupling element in Fig. 2. It is evident that the nonadiabatic coupling is comparable to the energy splitting and is often much larger. Therefore the adiabatic approximation does not generally hold and nonadiabatic effects can be expected to be observable in the spectrum. The full expressions for the linear and third-order response with the nonadiabatic coupling are given in Appendix D. The SLE provides an alternative route which circumvents the nonadiabatic simulations by expanding the phase space to include bath coordinates, as will be described below.

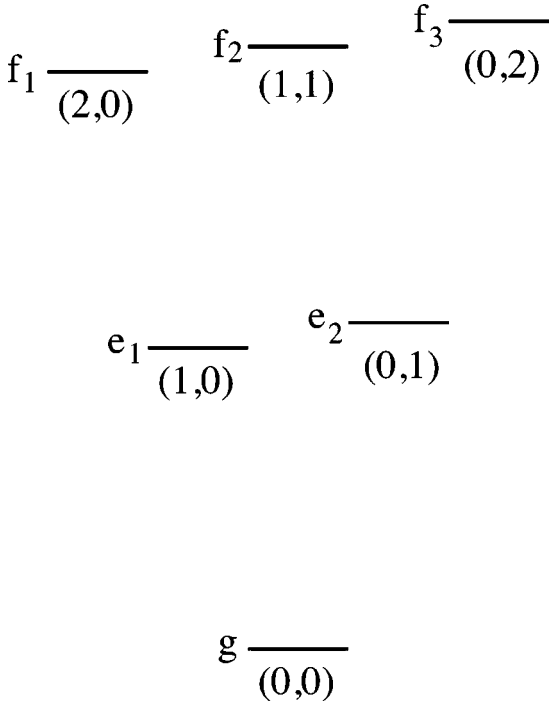

FIG. 3. Energy level diagram for the two amide I modes in trialanine. The excitation number of each mode is shown in parenthesis below each state.

III. THE LIOUVILLE EQUATION FOR TRIALANINE

Two local modes contribute to the amide I band of trialanine. The Hamiltonian is given in Eq. (1) with frequencies ω_a and ω_b, anharmonicities K_a and K_b, and the coupling constant J. A total of six levels will be considered. These are the ground state (g), two single excited levels (e_1 and e_2), and three doubly excited levels (f_1, f_2, and f_3),[67–69] as shown in Fig. 3. We denote a state, where the first mode (a) is excited n times and the second mode (b) is excited m times (n,m). m, $n=0,1,2$. The time evolution of the exciton system is determined by the Liouville equation

$$\frac{\partial}{\partial t}\boldsymbol{\rho}(t) = -\frac{i}{\hbar}\mathbf{L}(t)\boldsymbol{\rho}(t) - \frac{i}{\hbar}\mathbf{L}_{int}(t)\boldsymbol{\rho}(t), \quad (10)$$

where $\boldsymbol{\rho}$ is the density matrix describing the state of the two mode system. $\mathbf{L}(t)\rho(t) = -i/\hbar\,[H_0(t),\rho(t)]$ is the Liouvillian for the isolated system, while $\mathbf{L}_{int}(t)\rho(t) = -i/\hbar\,[H_{int}(t),\rho(t)]$ represents the coupling with the radiation field.

$L(t)$ does not couple states in different excitation manifolds (g, e, and f). Density matrix elements that do not have the same number of excitations in both the ket and the bra can then be treated separately. The density matrix can be

divided into independent blocks denoted ρ^{kj}, where k is the number of excitations in the ket and j the number of excitations in the bra, k, $j=0,1,2$. The Liouville operator corresponding to the density matrix block ρ^{kj} will be denoted $\mathbf{L}^{kj,kj}$:

$$\frac{\partial \rho^{kj}}{\partial t} = -\frac{i}{\hbar}\mathbf{L}^{kj,kj}\rho^{kj}. \tag{11}$$

For our model a total of eight blocks are needed to describe the third-order response, ρ^{gg}, ρ^{eg}, ρ^{ge}, ρ^{ee}, ρ^{fg}, ρ^{gf}, ρ^{fe}, and ρ^{ef}. Of those only five are independent, since $\rho^{\nu\nu'}$ and $\rho^{\nu'\nu}$ are Hermitian conjugates. The ground state density matrix $\rho^{gg}(t)=\rho_{gg}(t)$ evolves with the Liouville matrix

$$\mathbf{L}^{gg,gg}=[0]. \tag{12}$$

The density matrix elements with one excitation in the ket and the bra in the ground state,

$$\rho^{eg}(t)=\begin{pmatrix}\rho_{e_1g}(t)\\ \rho_{e_2g}(t)\end{pmatrix}, \tag{13}$$

evolves according to the Liouville matrix

$$\mathbf{L}^{eg,eg}=\begin{bmatrix}\omega_a & J\\ J & \omega_b\end{bmatrix}. \tag{14}$$

The evolution of the density matrix elements where both the ket and the bra are singly excited,

$$\rho^{ee}(t)=\begin{pmatrix}\rho_{e_1e_1}(t)\\ \rho_{e_1e_2}(t)\\ \rho_{e_2e_1}(t)\\ \rho_{e_2e_2}(t)\end{pmatrix}, \tag{15}$$

is determined by the Liouville matrix

$$\mathbf{L}^{ee,ee}=\begin{bmatrix}0 & -J & J & 0\\ -J & \omega_a-\omega_b & 0 & J\\ J & 0 & \omega_b-\omega_a & -J\\ 0 & J & -J & 0\end{bmatrix}. \tag{16}$$

The evolution of the density matrix elements with a doubly excited ket and a ground state bra,

$$\rho^{fg}(t)=\begin{pmatrix}\rho_{f_1g}(t)\\ \rho_{f_3g}(t)\\ \rho_{f_2g}(t)\end{pmatrix}, \tag{17}$$

is determined by the Liouville matrix

$$\mathbf{L}^{fg,fg}=\begin{bmatrix}2\omega_a-K_a & 0 & \sqrt{2}J\\ 0 & 2\omega_b-K_b & \sqrt{2}J\\ \sqrt{2}J & \sqrt{2}J & \omega_a+\omega_b\end{bmatrix}. \tag{18}$$

When the ket is doubly excited and the bra is singly excited the density matrix elements

$$\rho^{fe}(t)=\begin{pmatrix}\rho_{f_1e_1}(t)\\ \rho_{f_3e_1}(t)\\ \rho_{f_1e_2}(t)\\ \rho_{f_3e_2}(t)\\ \rho_{f_2e_1}(t)\\ \rho_{f_2e_2}(t)\end{pmatrix}, \tag{19}$$

the time evolution is determined by the Liouville matrix

$$\mathbf{L}^{fe,fe}=\begin{bmatrix}\omega_a-K_a & 0 & -J & 0 & \sqrt{2}J & 0\\ 0 & 2\omega_b-K_b-\omega_a & 0 & -J & \sqrt{2}J & 0\\ -J & 0 & 2\omega_a-K_a-\omega_b & 0 & 0 & \sqrt{2}J\\ 0 & -J & 0 & \omega_b-K_b & 0 & \sqrt{2}J\\ \sqrt{2}J & \sqrt{2}J & 0 & 0 & \omega_b & 0\\ 0 & 0 & \sqrt{2}J & \sqrt{2}J & 0 & \omega_a\end{bmatrix}. \tag{20}$$

The Liouville space dipole operator matrix elements are

$$M^{ab,cd}=\mu_{ac}\delta_{bd}-\mu_{bd}\delta_{ac}. \tag{21}$$

The time evolution of the density matrix elements with one excitation in the bra or the ket ρ^{ge} and ρ^{eg} determine the first time interval in the third-order nonlinear response (see Figs. 4–6). The second time interval is determined by ρ^{gg}, ρ^{ee}, and ρ^{fg} and the third time interval depends on the density matrix elements ρ^{eg} and ρ^{fe}.

IV. THE STOCHASTIC LIOUVILLE EQUATION

Many infrared experiments have been performed on the amide I band of trialanine. The absorption spectrum in D_2O has been measured at different pD values.[25,32,60,62] Woutersen and Hamm have reported the 2D IR pump probe spectrum of trialanine in D_2O at pD 1, where the molecule is fully protonated.[25,32] ^{13}C isotope labeling was used to further simplify the 2D IR spectrum.[26,28,32] These experiments suggested that trialanine primarily exists in the polyglycine II (P_{II}) structure in solution, a conformation characterized by Ramachandran angles of $(\psi,\phi)=(-60°,+140°)$.[25,26] However, significant α-helix like (α_R) composition was sug-

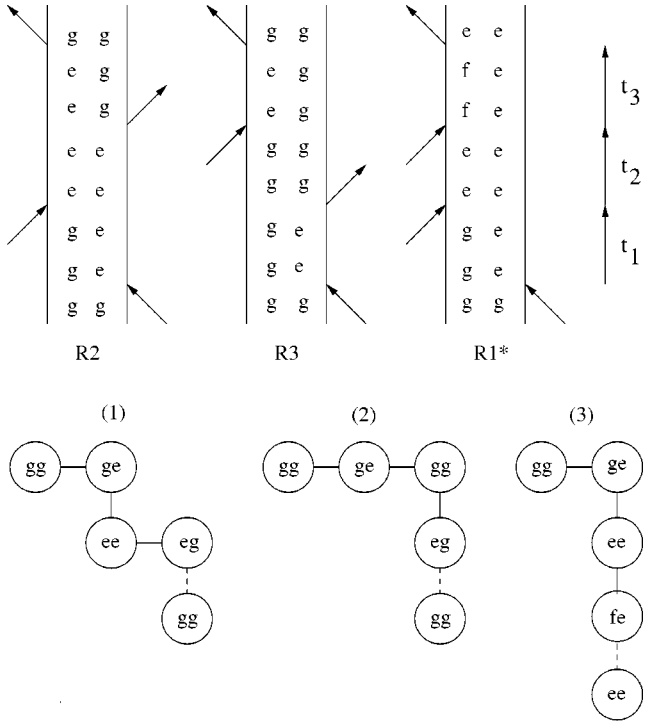

FIG. 4. Feynman diagrams and coupling schemes [(1) R_2, (2) R_3, and (3) R_1^*] for the photon echo (k_I). The ground state is denoted g. The single excited manifold is denoted e and the doubly excited manifold are denoted f.

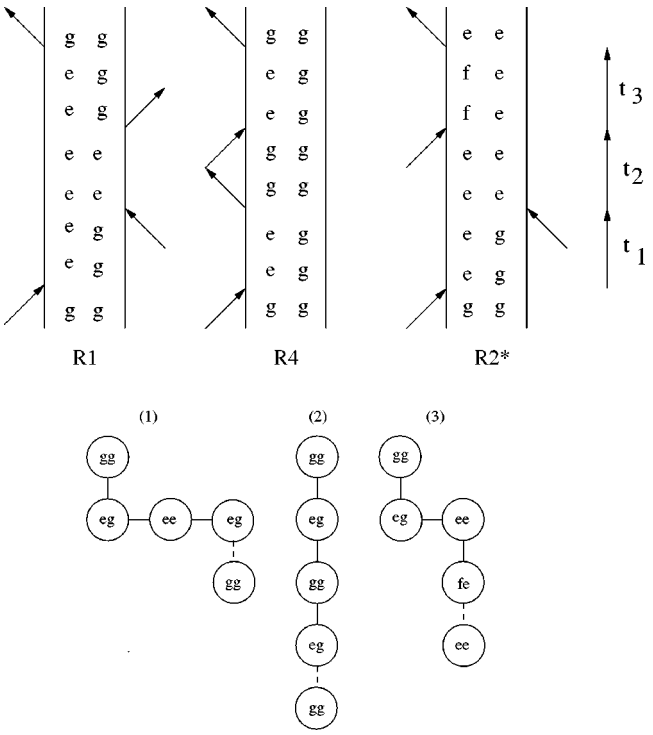

FIG. 5. Feynman diagrams and coupling schemes [(1) R_1, (2) R_4, and (3) R_2^*] for the $\mathbf{k}_{II}$ technique. The ground state is denoted g. The single excited manifold is denoted e and the doubly excited manifold is denoted f.

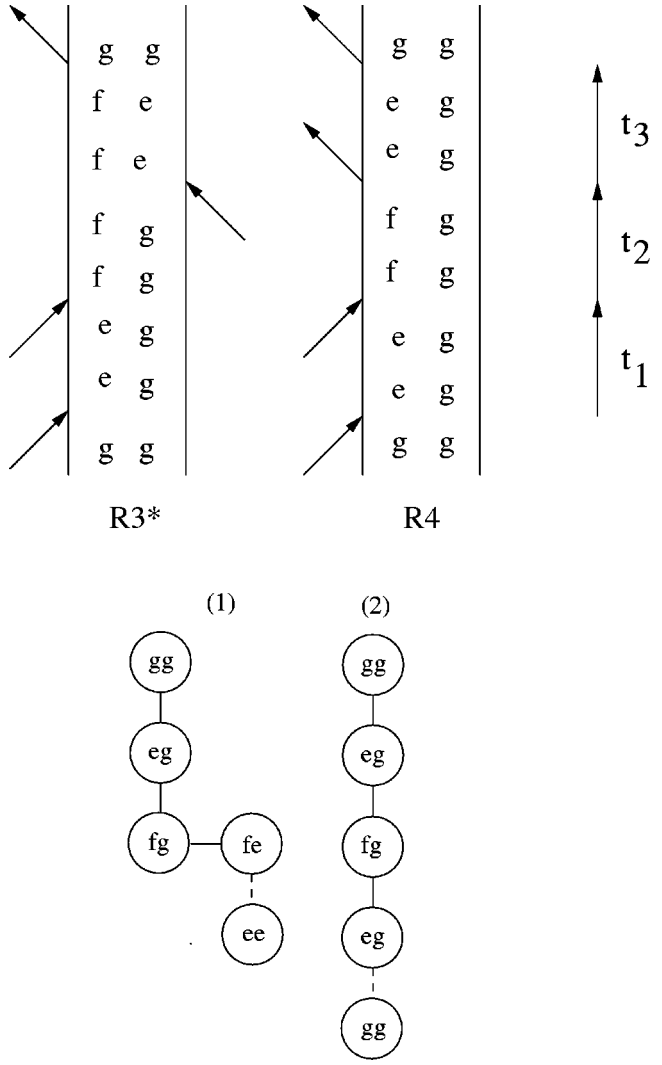

FIG. 6. Feynman diagrams and couplings schemes [(1) R_3^* and (2) R_4] for the $\mathbf{k}_{III}$ technique. The ground state is denoted g. The single excited manifold is denoted e and the doubly excited manifold is denoted f.

gested based on the spectral inhomogeneity of the amide I band.[28] In addition, the β strand conformation was suggested by polarized Raman and Fourier transform infrared (FTIR) experiments.[60,62]

Response functions expressed in terms of frequency fluctuation correlation functions of various functional forms were fitted to reproduce the experimental spectra.[25,28] The dephasing rate, central frequencies, and coupling constant were used as fitting parameters. The model assumes that the fluctuation of the coupling is so fast that motional narrowing ensures that the value can be approximated by the average value. Molecular dynamics simulations with various force fields[61,70,71] support the observation of a dominant P_{II} structure. However, different force fields predict the presence of both β strand and α_R structure as well and the relative stabilities of the different structures were found to be very sensitive to the force field parameters.

Our molecular dynamics simulation of trialanine in D_2O includes all the atoms of the trialanine and water. The aminoterminus group was protonated (see Fig. 1) to account for the experimental pD value of 1.[61,61] A chlorine counter ion

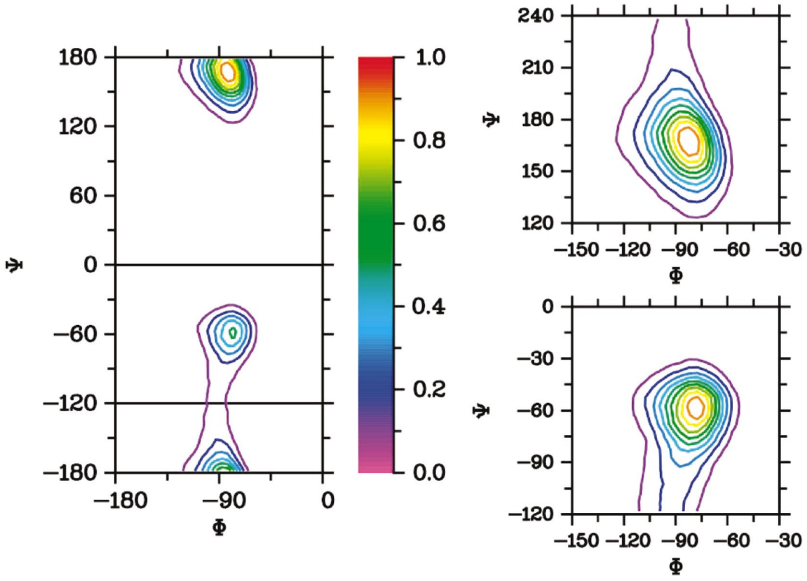

FIG. 7. (Color) The joint distribution of the Ramachandran angles. The nine coloured equidistant contour lines are plotted. The horizontal black lines at $\psi=0°$ and $\psi=-120°$ indicate the boundary used to distinguish between the P_{II} and α_R configurations. P_{II} is centered around $\psi=170°$ while α_R is centered around $\psi=-60°$. To the right is the close up of the P_{II} (top) and α_R (bottom) areas of the Ramachandran angle joint distribution plot. Angles between 180° and 240° in the plot for P_{II} correspond to angles between $-180°$ and $-120°$ equivalent to a full 360° rotation.

was added to the simulation box to keep the system neutral. The initial trialanine structure was obtained from the MAESTRO package.[72] The velocity Verlet algorithm[73] was used to describe the motion of the system. The CHARMM27 force field was employed for all interactions with a cutoff of 10 Å for the nonbonded interactions. The Ewald Sum[74] was used to calculate the long range electrostatic interactions. The simulation was carried using the CHARMM package.[75] The structure was first refined in vacuum using a 3000 step energy minimization procedure, PRCG from the MAESTRO package.[72] The molecule was then embedded in a cubic unit cell of TIP3 water[76] with the length of box 32 Å. The cutoff distance for the Lennard-Jones forces was set to 12 Å. All the water molecules overlapping with the trialanine were removed. The system includes one trialanine and 971 water molecules. To release the internal tension, a 10 000 steps Adopted Basis Newton-Raphson[75] energy minimization was performed. The system was then equilibrated under NPT ensemble with 1/fs time step for 1 ns to get the right density and box size, the extended system method[77–79] was used to keep the temperature and pressure constant, the final box length is 30.4 Å. This was followed by an equilibration of the system in the NVE ensemble with 1 fs time step for 1 ns. After the equilibration phase, a 10 ns analysis trajectory was obtained by applying the NVE ensemble with 1 fs time steps. The structure was saved for every 10 fs giving a total of 10^6 sample points.

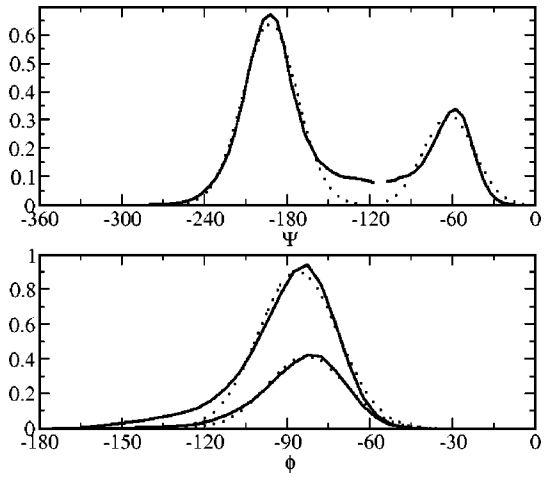

FIG. 8. The distribution of the Ramachandran angles. Solid lines are simulated data and dotted lines are Gaussian fits. Upper panel—the ψ distribution, P_{II} is the left peak around 180°. α_R is the small right peak at $-60°$. Lower panel—the ϕ distribution, both configurations now peak around 80°. The larger peak (P_{II} configuration) the small peak (α_R configuration).

The joint distribution of the Ramachandran angles is shown in Fig. 7. The two peaks correspond to a P_{II} and an α_R configuration. Configurations with $-120°<\psi<0°$ were assigned as α_R, while all other configurations were taken as P_{II}. These boundaries between the two configurations are indicated by black lines in Fig. 7. Interconversion between the two species takes place when ψ crosses the barrier around $-120°$. We found the P_{II} configuration for 70% of the time and α_R for the remaining 30%. These are comparable to the similar simulations of Stock and co-workers.[61] Those authors found, however, a large variation in the relative abundance of different configurations of trialanine with different force fields (AMBER, CHARMM, GROMOS, and OPLS). This discrepancy was also reported for other small peptides.[80,81] The calculated abundance should thus be treated with some caution and spectra will therefore be presented both for the individual configurations and the mixture.

The distribution functions of the Ramachandran angles obtained for each configuration were fitted to Gaussians. The simulations and fits are shown in Fig. 8. The average values and variances Δ^2 are reported in Table I. The average angle between the CO transition dipoles (Θ) is reported in Table I

TABLE I. Distribution parameters for the two configurations of trialanine.

Configurations	$\langle\phi\rangle$ (deg)	Δ_ϕ (deg^2)	$\langle\psi\rangle$ (deg)	Δ_ψ (deg^2)	Θ (deg)	Pop.
P_{II}	−86.0	14.3	167.4	20.1	113.9	70%
α_R	−82.9	14.1	−62.7	18.3	85.4	30%

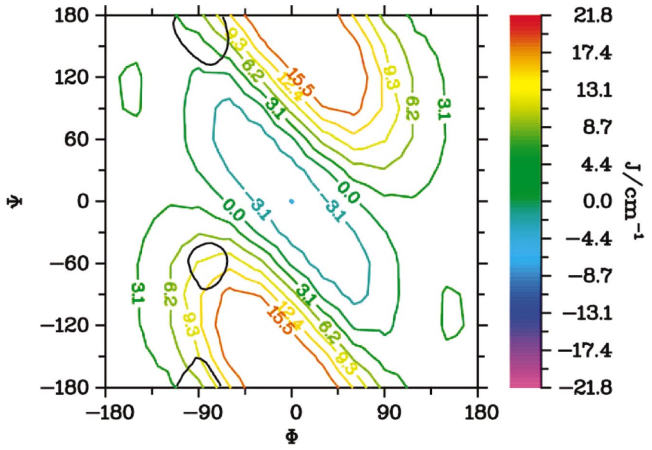

FIG. 9. (Color) Ramachandran plot of coupling constant from Ref. 64. The black contour lines are drawn for 25% of the peak value of the joint distribution of the Ramachandran angles.

as well. The distribution of Ramachandran angles are superimposed on the Tasumi *ab initio* map[64] for the coupling J_{ab} in Fig. 9. In Fig. 10 the distributions of the coupling in the two configurations are shown along with the distribution of the frequencies.

The two configurations are found to be quite stable and only 38 transitions occur during the 10 ns simulation. This indicates that the lifetimes of the two species are a few hundred picoseconds. The slow exchange between the two configurations should not affect line shapes. We thus neglected this dynamics and calculated the response as the inhomogeneous average of the response of the individual species. The correlation functions of the Ramachandran angles were calculated for 350 ps pieces of the trajectory, where the system was in the same configuration all the time. The correlation functions were well fitted by biexponentials with a fast 100 fs decay and a slower 4 ps decay as shown in Fig. 11 (see Table II).

The probability distribution $P(\mathbf{\Omega},t)$ is assumed to satisfy the Markovian master equation (see Appendix A)

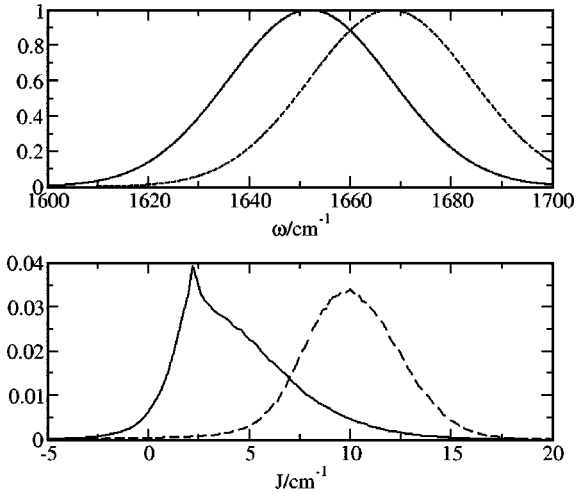

FIG. 10. Top: distribution of the frequencies for the low (solid) and high (dashed) frequency CO stretch. Bottow: distribution of the coupling for P_{II} (solid) and α_R (dashed).

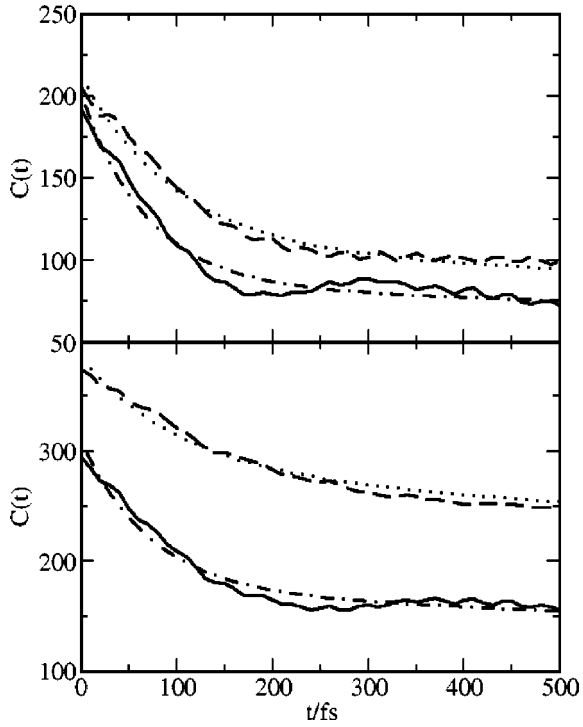

FIG. 11. The calculated correlation functions of the Ramachandran angles. Solid lines and dash-dotted lines are the calculated and fitted correlation functions of ϕ. Dashed and dotted lines are the calculated and fitted correlation functions of ψ. The fitting parameters are given in Table II.

$$\frac{\partial P(\mathbf{\Omega},t)}{\partial t} = -\Gamma(\mathbf{\Omega})P(\mathbf{\Omega},t) \tag{22}$$

with $\Omega_1=\delta\omega_a$, $\Omega_2=\delta\omega_b$, $\Omega_3=\delta\phi$, and $\Omega_4=\delta\psi$. $\Gamma(\mathbf{\Omega})$ is the relaxation operator for the stochastic variables $\mathbf{\Omega}$. The Smoluchowski equation for our Brownian oscillator model is

$$\frac{\partial P(\mathbf{\Omega},t)}{\partial t} = -\sum_{j=1}^{4} \gamma_j \frac{\partial}{\partial \Omega_j}\left(\Omega_j + \Delta_j^2 \frac{\partial}{\partial \Omega_j}\right) P(\mathbf{\Omega},t). \tag{23}$$

Four independent collective coordinates were chosen to represent the relevant bath motion. Each coordinate is modeled as a Brownian oscillator and has two parameters Δ (distribution) and γ (relaxation constant). The frequency shifts from the average value of the fundamental frequency for each mode ($\delta\omega_a$ and $\delta\omega_b$) are treated as independent stochastic

TABLE II. Parameters for the SLE.

	P_{II}	α_R	fit A	fit B
ω_a (cm^{-1})	1652	1652	1647.41	1649.48
ω_b (cm^{-1})	1668	1668	1672.18	1672.54
γ_{ω_a} (ps^{-1})	4.545	4.545	4.344	6.281
Δ_{ω_a} (cm^{-1})	16.1	16.1	19.614	22.951
γ_{ω_b} (ps^{-1})	4.545	4.545	4.916	4.909
Δ_{ω_b} (cm^{-1})	16.1	16.1	19.836	20.826
$\langle\phi\rangle$ (deg)	−86.0	−82.9	−80.5	−83.6
γ_ϕ (ps^{-1})	13.53	14.57	11.474	⋯
Δ_ϕ (deg^2)	14.3	14.1	9.886	⋯
$\langle\psi\rangle$ (deg)	167.4	−62.7	165.9	163.8
γ_ψ (ps^{-1})	9.55	10.08	4.315	⋯
Δ_ψ (deg^2)	20.1	18.3	19.014	⋯

TABLE III. The expansion coefficients for the coupling in terms of the deviations of the Ramachandran angles from the average values in the two configurations. The units are $\mathrm{cm}^{-1}\,\mathrm{deg}^{-n}$, where n depends on the order of the expansion coefficient.

	P_{II}	α_R
C_{00}	4.039 94	10.5145
C_{10}	0.143 177	0.089 882 9
C_{01}	0.125 022	−0.115 885
C_{11}	$2.831\,73\times10^{-3}$	$-2.946\,88\times10^{-3}$
C_{20}	$2.434\,53\times10^{-3}$	-1.0161×10^{-3}
C_{02}	$4.443\,14\times10^{-4}$	$-6.869\,57\times10^{-4}$
C_{21}	$4.288\,92\times10^{-6}$	$1.756\,54\times10^{-5}$
C_{21}	$-1.756\,13\times10^{-5}$	-7.1161×10^{-6}
C_{22}	$-5.127\,53\times10^{-7}$	-1.2963×10^{-10}

variables. These fluctuations are dominated by the interaction with the solvent water molecules in the vicinity of each individual amide unit. The Brownian oscillator parameters for the frequencies are $\gamma_a^{-1}=\gamma_b^{-1}=220$ fs and $\Delta_a=\Delta_b=16.1\ \mathrm{cm}^{-1}$, which were found to reproduce the experimental line shape for the isolated amide I mode in NMA.[57] The fundamental frequencies are given by $\omega_a=\langle\omega_a\rangle+\delta\omega_a$ and $\omega_b=\langle\omega_b\rangle+\delta\omega_b$. The average frequencies ($\langle\omega_a\rangle$ and $\langle\omega_b\rangle$) for the two bands were taken to be 1652 and 1668 cm^{-1}, respectively.[32,62] The difference is due to the charge on the terminal amino group and the amide unit closest to the acid group has the lowest frequency (see Fig. 1).

The intermode coupling J between the two modes is determined mainly by the Ramachandran angles. The fluctuations of these angles ($\delta\phi$ and $\delta\psi$) are a natural choice of stochastic variables for the coupling. The coupling J was expanded in the Ramachandran angle fluctuations ($\delta\phi$ and $\delta\psi$),

$$J(\delta\phi,\delta\psi)=\sum_{i=0}^{2}\sum_{j=0}^{2}C_{ij}\delta\phi^i\delta\psi^j, \tag{24}$$

where C_{ij} are the expansion coefficients. C_{00} is the coupling at the average position of the Ramachandran angles around which the Taylor expansion is made. We found $C_{00}=4\ \mathrm{cm}^{-1}$ in the P_{II} configuration and $10.5\ \mathrm{cm}^{-1}$ for α_R. C_{ij} were obtained by a fit to the Tasumi map connecting the coupling constant and the Ramachandran angles.[64] The remaining expansion coefficients are reported in Table III. The stochastic variables ($\delta\omega_a$, $\delta\omega_b$, $\delta\phi$, and $\delta\psi$) are all treated as Brownian oscillators using the relaxation operator given in Appendix C. The parameters for the Brownian oscillator models used for the Ramachandran angles were taken from the fits of the Ramachandran angle auto correlation functions as reported in Table II.

The stochastic Liouville equation is constructed by combining the Liouville equation for the exciton system [Eq. (10)] and the Markovian master equation [Eq. (22)] for the four collective Brownian oscillator coordinates:

$$\dot{\boldsymbol{\rho}}(\boldsymbol{\Omega},t)=-\frac{i}{\hbar}\mathbf{L}(\boldsymbol{\Omega})\boldsymbol{\rho}(\boldsymbol{\Omega},t)-\Gamma(\boldsymbol{\Omega})\boldsymbol{\rho}(\boldsymbol{\Omega},t). \tag{25}$$

The frequencies and coupling for the exciton system described in Sec. III undergo fluctuations depending on the collective bath coordinates $\boldsymbol{\Omega}$ defined in Sec. IV whose coupling with the system is given by the $\boldsymbol{\Omega}$ dependence of $\mathbf{L}(\boldsymbol{\Omega})$. Fluctuations of the anharmonicities K_a and K_b are neglected and we set $K_a=K_b=16\ \mathrm{cm}^{-1}$.[31,58,82] The transition dipoles for the two modes were placed at the C–O bond 0.8268 Å from the carbon atom forming an angle of 20° with the bond.[83] Fluctuation of the transition dipoles of the local modes were neglected and their magnitude was set to unity.

V. THE LINEAR ABSORPTION

The solution of the stochastic Liouville equation is outlined in Appendix A. The evolution of the kj block of the SLE is expressed in terms of the Green's function $\mathcal{G}^{kj}(\boldsymbol{\Omega},\boldsymbol{\Omega}',t)$,[52]

$$\boldsymbol{\rho}^{kj}(\boldsymbol{\Omega},t)=\int\mathcal{G}^{kj,kj}(\boldsymbol{\Omega},\boldsymbol{\Omega}',t)\boldsymbol{\rho}^{kj}(\boldsymbol{\Omega}',0)d\boldsymbol{\Omega}'. \tag{26}$$

The procedure used to obtain the Green's function in the frequency domain is given in Appendix E. The response functions are given in terms of the Green's function in Appendix B.

The absorption line shapes [Eq. (B1)] were simulated at four levels of sophistication. At the highest level (i), fluctuations of all four collective bath coordinates as described in Sec. IV are included. At this level the Liouvillian is constructed in the local basis and the coupling between the two local modes fluctuates depending on the Ramachandran angles. The local mode frequencies fluctuate as well. At the next level (ii) the coupling is held fixed and only the local mode frequencies are fluctuating. The importance of the Ramachandran angle fluctuations is revealed by comparing these two levels. At the third level (iii) the Liouvillian is constructed in the fixed average Hamiltonian eigenbasis and only the eigenvalues are allowed to fluctuate. The fourth level (iv) is identical to (iii) except the fluctuations of the diagonal elements in the exciton basis are taken to be very slow. In practice, as the frequency fluctuations become slow a larger basis is needed to ensure the convergence of continued fraction solution to the SLE. For faster convergence in the static simulations (iv) the time scale for the fluctuations have been set an order of magnitude longer than in (iii).

The linear absorption of P_{II} is given in Fig. 12 for the four models. In model (iv) the spectrum is one broad Gaussian centerd at 1660 cm^{-1}. In model (iii) the two peaks are resolved. The stronger peak is around 1650 cm^{-1} and the weaker at 1670 cm^{-1}. Model (ii) is very similar to (iii). The low frequency peak gain a bit of intensity, while the high frequency peak loose a bit. In model (i) the two peaks get closer and the low frequency peak intensity decreases.

The linear response of α_R is also given in Fig. 12. In model (iv) a broad Gaussian line is observed around 1660 cm^{-1}. In the spectrum for model (iii) two peaks are visible at 1645 cm^{-1} and 1675 cm^{-1}. Here the highest frequency peak is the strongest. In model (ii) the peaks move slightly apart and they both gain intensity. In model the high frequency peak gain intensity.

In model (iii) there is no coupling between the two modes, the eigenstates are time independent and the nonadia-

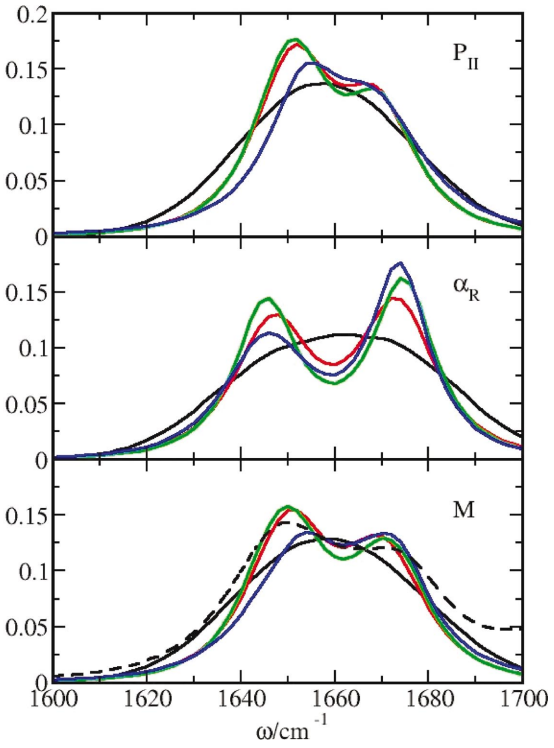

FIG. 12. (Color) The linear absorption of P_{II}, α_R, and M. Blue model (i) absorption; green model (ii); red model (iii); black model (iv). The black dashed line in the lower panel is the experimental spectrum (Ref. 32).

batic coupling elements vanish. In model (ii) the coupling between the two modes is finite and the eigenstates will be time dependent and the nonadiabatic coupling elements is finite. The difference between these two models illustrates the effect of the nonadiabatic coupling, when the coupling fluctuations are neglected. In general we expect that a weak peak can borrow intensity from other peaks through the nonadiabatic coupling. This is observed in the linear absorption for both configurations.

The two conformations have different linear absorption spectra with a smaller Davydov splitting in P_{II}. Further, the low frequency peak is generally the most intense in the P_{II} conformation, while the reverse is true for α_R. The two species interchange on a 100 ps time scale. The linear absorption for a 70/30 mixture (M) of P_{II} and α_R are presented and compared with experiment in Fig. 12. In the experimental spectrum the low frequency peak is the strongest, while in the combined spectrum the two peaks seem equally strong and the simulated low frequency peak has a slightly higher frequency compared to experiment.

The linear response was fitted using simplex minimization[84] of the root mean square deviation between a single configuration SLE simulation and experiment.[32] The fit is not unique and two fits were obtained. All 12 parameters used in the SLE were optimized in fit *A*. Eight parameters were used in fit *B*, where the Ramachandran angles were kept fixed. The fits are shown in Fig. 13 and the parameters are given in Table II. The tail of the carboxyl CO stretch peak at 1725 cm^{-1} observed in the high frequency end of the spectrum was not included in the fits. The geometries of the configurations obtained with the fits are similar to the geometry P_{II}.

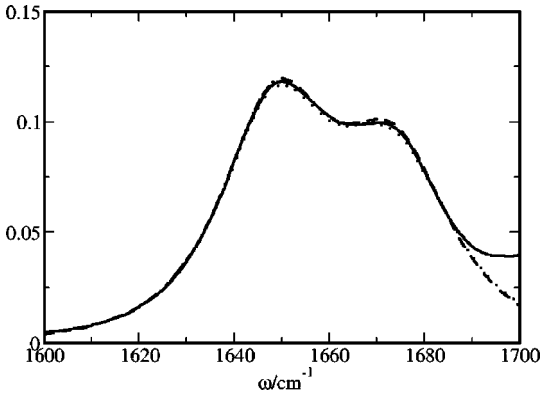

FIG. 13. The fitted linear absorption. The solid line is experiment. The dotted line is fit *A* and the dashed line is fit *B*. The deviation at high frequencies is due to the carbonyl group CO stretch that is not included in the simulation.

VI. THE THIRD-ORDER RESPONSE

Simulations were carried out for three signals generated in the directions: $\mathbf{k}_I=-\mathbf{k}_1+\mathbf{k}_2+\mathbf{k}_3$, $\mathbf{k}_{II}=\mathbf{k}_1-\mathbf{k}_2+\mathbf{k}_3$ and $\mathbf{k}_{III}=\mathbf{k}_1+\mathbf{k}_2-\mathbf{k}_3$.[35,85] $\mathbf{k}_1$, $\mathbf{k}_2$, and $\mathbf{k}_3$ are the wave vectors of the three laser pulses. In Figs. 4–6 the Feynman diagrams and coupling schemes for the three techniques are shown. The pulse sequences for the three techniques are shown in Fig. 14. All techniques use short laser pulses that are resonant with both the *ge* and *ef* transitions. The expressions used in the simulations are given in Appendix B [Eqs. (B13), (B17), and (B21)]. The simulations were performed in the frequency domain where all plots are presented for the imaginary parts or the response:

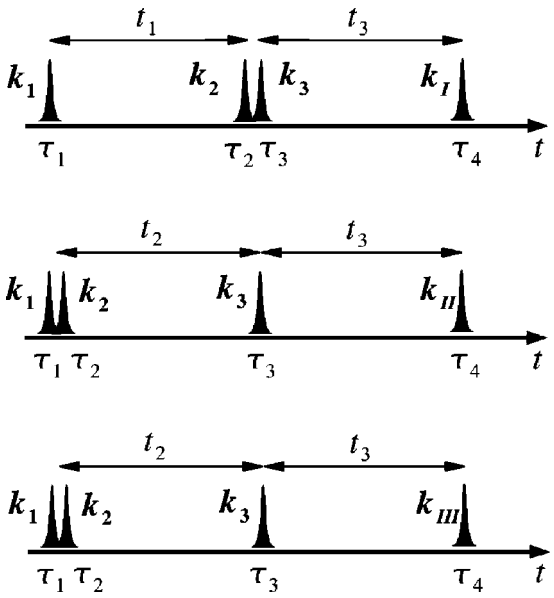

FIG. 14. Pulse sequences for the three techniques. From top to bottom, $\mathbf{k}_I$ (photon echo), $\mathbf{k}_{II}$, and $\mathbf{k}_{III}$ (reversed photon echo).

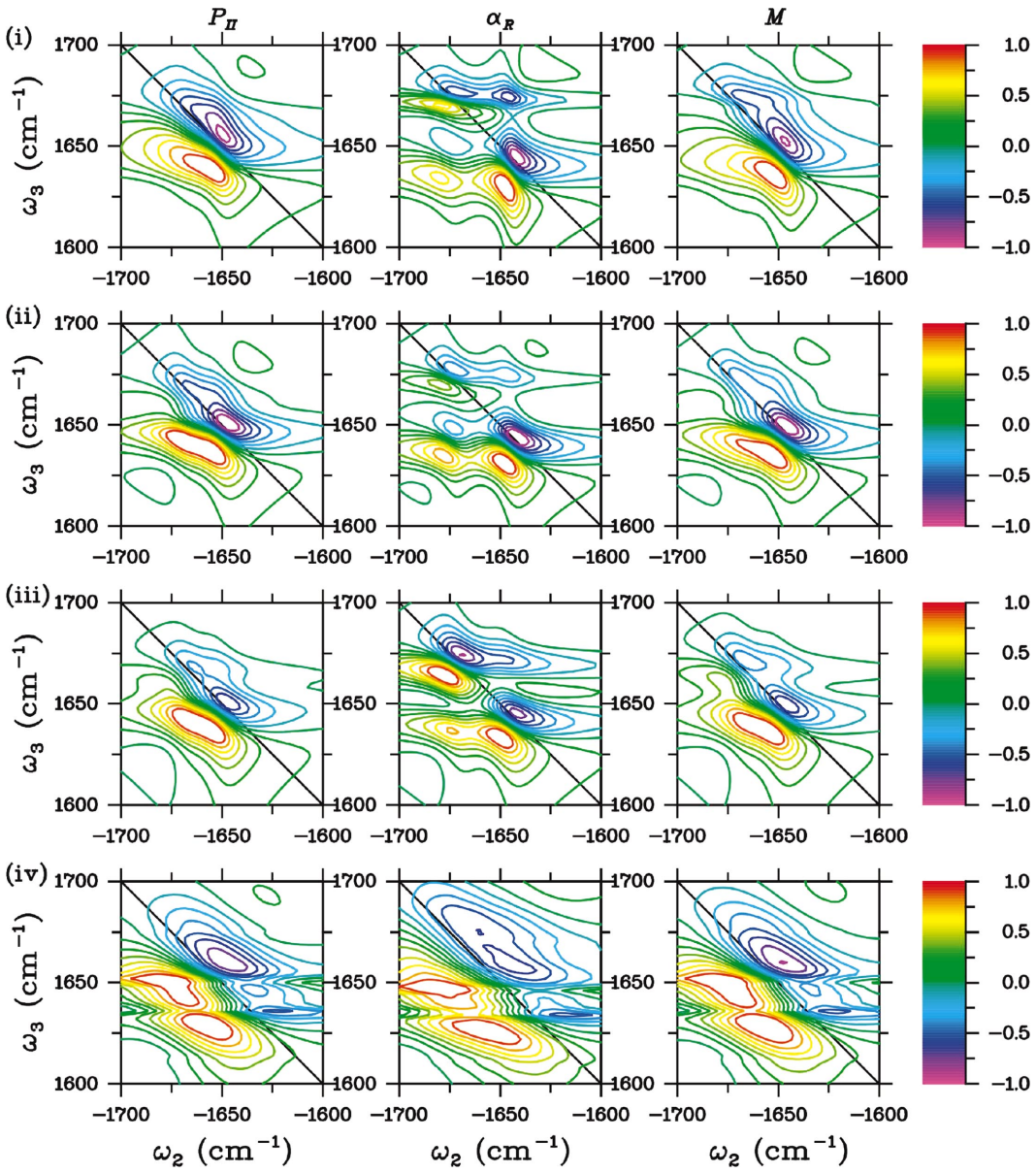

FIG. 15. (Color) The photon echo spectra S^I_{ZZZZ}. From left to right spectra of P_{II}, α_R, and M are shown. From top to bottom model (i), (ii), (iii), and (iv). Blue colors are negative and red colors are positive. All spectra are normalized to the most intense peak.

$$S^I(\omega_1,t_2,\omega_3)=\mathrm{Im}\int_{-\infty}^{\infty}d\omega_2 S^I(\omega_1,\omega_2,\omega_3)\times\exp(-i\omega_2 t_2), \tag{27}$$

$$S^{II}(t_1,\omega_2,\omega_3)=\mathrm{Im}\int_{-\infty}^{\infty}d\omega_1 S^{II}(\omega_1,\omega_2,\omega_3)\times\exp(-i\omega_1 t_1), \tag{28}$$

$$S^{III}(t_1,\omega_2,\omega_3)=\mathrm{Im}\int_{-\infty}^{\infty}d\omega_1 S^{III}(\omega_1,\omega_2,\omega_3)\times\exp(-i\omega_1 t_1). \tag{29}$$

The 2D IR spectra depend on the polarization directions of the laser pulses[23,86] and were calculated for two configurations. In the first all fields and the signal are parallel ($ZZZZ$) and in the second pulses 1 and 2 are perpendicular to pulse 3 and the signal ($ZZYY$). The spectra were calculated in the molecular frame and then averaged over the orientations in the laboratory frame using Eq. (7) of Ref. 23.

The photon echo spectra S^I_{ZZZZ} [Eq. (B14)] are shown in Fig. 15. For P_{II} all four models i, ii, iii, and iv have negative peaks above the diagonal and positive peaks below the diagonal. In the static limit (iv) multiple overlapping peaks are observed, while in all other cases one peak is found above the diagonal and one below. These peaks are stretched out along the diagonal. While the spectra for models (iii) and (ii) look very similar, the model (i) spectrum has sharper peaks that are less stretched out along the diagonal. The spectra of α_R show multiple peaks above and below the diagonal. Pairs of positive and negative peaks are located at the diagonal positions $(\omega_1=-1650\ \mathrm{cm}^{-1},\omega_3=1650\ \mathrm{cm}^{-1})$ and $(\omega_1=-1670\ \mathrm{cm}^{-1},\omega_3=1670\ \mathrm{cm}^{-1})$. Cross peaks are located at $(\omega_1=-1650\ \mathrm{cm}^{-1},\omega_3=1670\ \mathrm{cm}^{-1})$ and $(\omega_1$

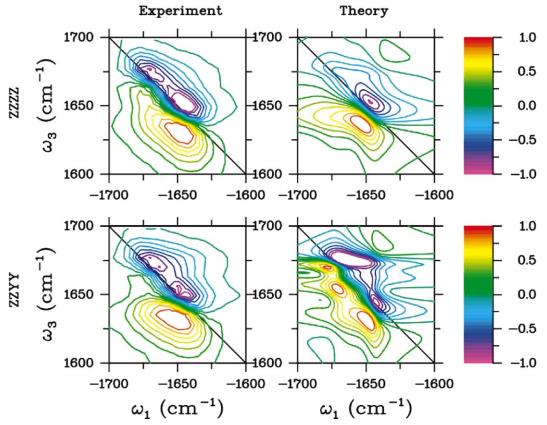

FIG. 16. (Color) The experimental S^I photon echo spectrum corresponding (left) of trialanine (Ref. 25) and the simulated model (i) spectrum (right). The spectra for parallel pulses are shown at the top and for perpendicular at the bottom. Blue colors are negative and red colors are positive. The spectra are normalized to the most intense peak.

$=-1670\ \text{cm}^{-1}, \omega_3=1650\ \text{cm}^{-1}$). For model (iv) these peaks strongly overlap. In the spectrum for model (iii) the diagonal peaks are approximately equally strong, while the low frequency diagonal peak is the strongest in the model (ii) spectrum. For model (i) the negative part of the cross peak above the diagonal is the most intense. The mixture (M) spectra of the two configurations are dominated by P_{II}, but a series of weak extra peaks are observed at the ($\omega_1=-1670\ \text{cm}^{-1}, \omega_3=1670\ \text{cm}^{-1}$) diagonal position. In the spectra observed by Woutersen and Hamm[25,32] shown in Fig. 16 together with the model (i) spectrum of the mixture these diagonal peaks are more pronounced. Note that the experimental spectrum was obtained with a time delay t_2 of 1.5 ps, where the delay time in the simulation is 0 ps.

The simulated S^I_{ZZYY} spectra are shown in Fig. 17. For P_{II}, model (iv) shows a broad positive going peak with some structure below the diagonal and a broad negative peak is observed above the diagonal. Model (iii) gives two sharp

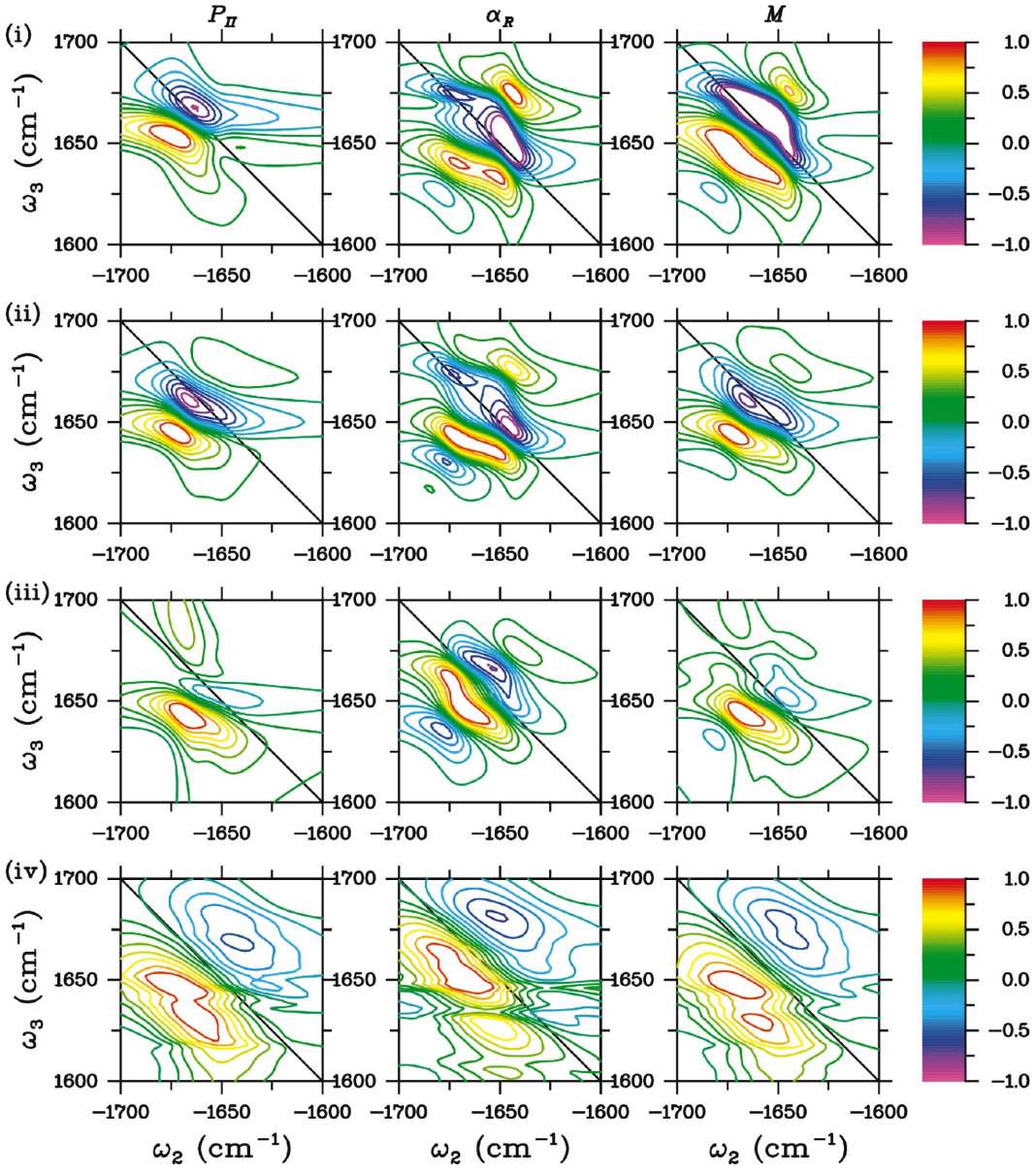

FIG. 17. (Color) Same as Fig. 15 but for S^I_{ZZYY}.

peaks one above the diagonal and one below. The two strong peaks are predominantly the cross peaks at ($\omega_1 = -1650\ \mathrm{cm}^{-1}$, $\omega_3 = 1670\ \mathrm{cm}^{-1}$) and ($\omega_1 = -1670\ \mathrm{cm}^{-1}$, $\omega_3 = 1650\ \mathrm{cm}^{-1}$). Between these a number of weaker features are observed, arising from interference between the negative part of the cross peak below the diagonal and the positive going cross peak above the diagonal. For model (ii) the cross peak below the diagonal and the low frequency diagonal peak dominate the spectrum. Weaker features are observed above the diagonal. Model (i) shows only two peaks, one above and one below the diagonal. Located around ($\omega_1 = -1660\ \mathrm{cm}^{-1}, \omega_3 = 1660\ \mathrm{cm}^{-1}$) they look like the response from one mode rather than two. For α_R the model (iv) response is again the broadest and dominated by the diagonal peak around 1670 cm^{-1}. In the remaining spectra the peaks are sharper and weak cross peaks are observed. For model (ii) the low frequency diagonal peak is the strongest. For model (i) the two diagonal peaks are equally strong again.

For M, multiple peaks are observed in all spectra. Model (i) gives three positive peaks below the diagonal. The peaks at the lowest and highest frequency predominantly comes from α_R, while the middle peak comes from P_{II}. Above the diagonal two negative peaks are observed. The high frequency peaks is a combination of peaks from α_R and P_{II}, while the low frequency peak predominantly comes from α_R. In the experimental spectrum[25,32] shown in Fig. 16 only one peak is observed below the diagonal. Above the diagonal two peaks are observed. These peaks both seem to be split into two peaks, but this splitting is not very pronounced and might be due to the limited time resolution in the experiment. Below the diagonal only one peak is observed in contrast to the three in the simulated model (i) spectrum. Note that the experimental spectrum was obtained with a time delay t_2 of 1.5 ps, where the delay time in the simulation is 0 ps.

The simulated linear response and 2D IR spectra did not perfectly match experiment. A comparison with experiment suggests that the α_R component is overestimated by the molecular dynamics simulation. An earlier study by Stock and co-workers[61] showed that different molecular dynamics force fields predict very different probabilities for the different conformations of trialanine. The Ramachandran angles obtained from the molecular dynamics trajectories may not be sufficiently accurate. However, the present method need not necessarily rely on molecular dynamics simulations. For example parameters obtained from NMR can be used.

The S^{II}_{ZZZZ} spectra [Eq. (B18)] with $t_1 = 0$ for the four models are shown for P_{II}, α_R, and M in Fig. 18. In all cases the peaks are stretched along the $\omega_2 = 0$ axis. Little difference is observed between the four models for P_{II}. For α_R the main peaks are split into two when going from model (iv) to model (iii). In model (ii) and model (i) spectra the lower of the split peaks is the strongest.

The S^{II}_{ZZYY} spectra with $t_1 = 0$ for configuration P_{II}, α_R, and M are given in Fig. 19 for the four models. In all spectra the peaks are stretched along the axis, where $\omega_2 = 0$. The number of peaks varies for the different models in both the P_{II} and α_R configurations.

The S^{III}_{ZZZZ} spectra [Eq. (B22)] for P_{II}, α_R, and M are given in Fig. 20. In this technique the fg elements show up along the ω_2 axis and the fe and eg density matrix elements along the ω_3 axis. The three fg elements have frequencies around 3287 (3281) cm^{-1} f_1g, 3326 (3337) cm^{-1} f_2g, and 3315 (3309) cm^{-1} f_3g for $P_{II}(\alpha_R)$. The fe elements have frequencies around 1636 (1635) cm^{-1} f_1e_1, 1675 (1690) cm^{-1} f_2e_1, 1618 (1608) cm^{-1} f_1e_2, 1657 (1664) cm^{-1} f_2e_2, 1646 (1636) cm^{-1} f_3e_1, and 1664 (1663) cm^{-1} f_3e_2 for $P_{II}(\alpha_R)$. The dominant peaks are those where the system is in the f_1g state during t_2 and in f_1e_1 or e_1 during t_3 and those where the system is in the f_3g state during t_2 and in f_3e_2 or in e_2g during t_3. Negative peaks at the f_3g, e_1g position and f_1g, e_2g are observed in some spectra as well. The S^{III}_{ZZYY} spectra for P_{II}, α_R, and M are depicted in Fig. 21. For P_{II} and α_R the number of resolved peaks reduces from model (iii) to model (ii). The difference between (ii) and (i) is less pronounced. In P_{II} model (i) there are two peaks along the ω_2 axis. The negative peak in the middle between the two fundamental frequencies results from motional narrowing. The stretch along ω_2 indicates that all three fg elements are reached. For α_R the peaks merge when going from model (iii) to (i) creating four peaks with approximately the same ω_2 frequency in model (i) again indicating motional narrowing.

VII. DISCUSSION

The simulated linear absorption showed some differences with experiment. For model (i) the intensity of the high frequency peak is overestimated. This suggests that the MD simulation overestimates the abundance of the α_R configuration, in agreement with the conclusions reached by others.[25,26,32,62] By varying the relative weight of the two configurations we found better agreement as the weight of α_R is lowered. When fitting all parameters to the linear absorption (fits A and B) only one P_{II} configuration was needed.

The total simulated S^{I}_{ZZZZ} spectrum has two equally strong peaks, while in the experimental spectrum shown in Fig. 12 the lowest frequency peak is slightly stronger, more resembling P_{II} than the α_R configuration. The experimental spectrum shown in Fig. 16 was reproduced reasonably well in the full simulation. The weak peak observed experimentally around ($\omega_1 = -1670\ \mathrm{cm}^{-1}, \omega_3 = 1670\ \mathrm{cm}^{-1}$) is, however, missing. The simulated S^{I}_{ZZYY} spectrum shows multiple positive α_R peaks below the diagonal that are not observed in the experimental spectrum.

Several factors contribute to the differences between the simulated and experimental spectra. First the 30% probability of finding the system in α_R may be too high. In the light of the recent study by Stock and co-workers[61] reporting very strong population dependence of the different conformations on the force fields this is likely. However, the simulated P_{II} spectrum does not provide a perfect match either. The low frequency peak has a slightly higher frequency in the simulated spectrum. These might be due to some of the simplifications in the model such as the neglect of coupling to other modes as the carbonyl stretch in the acid group. Furthermore,

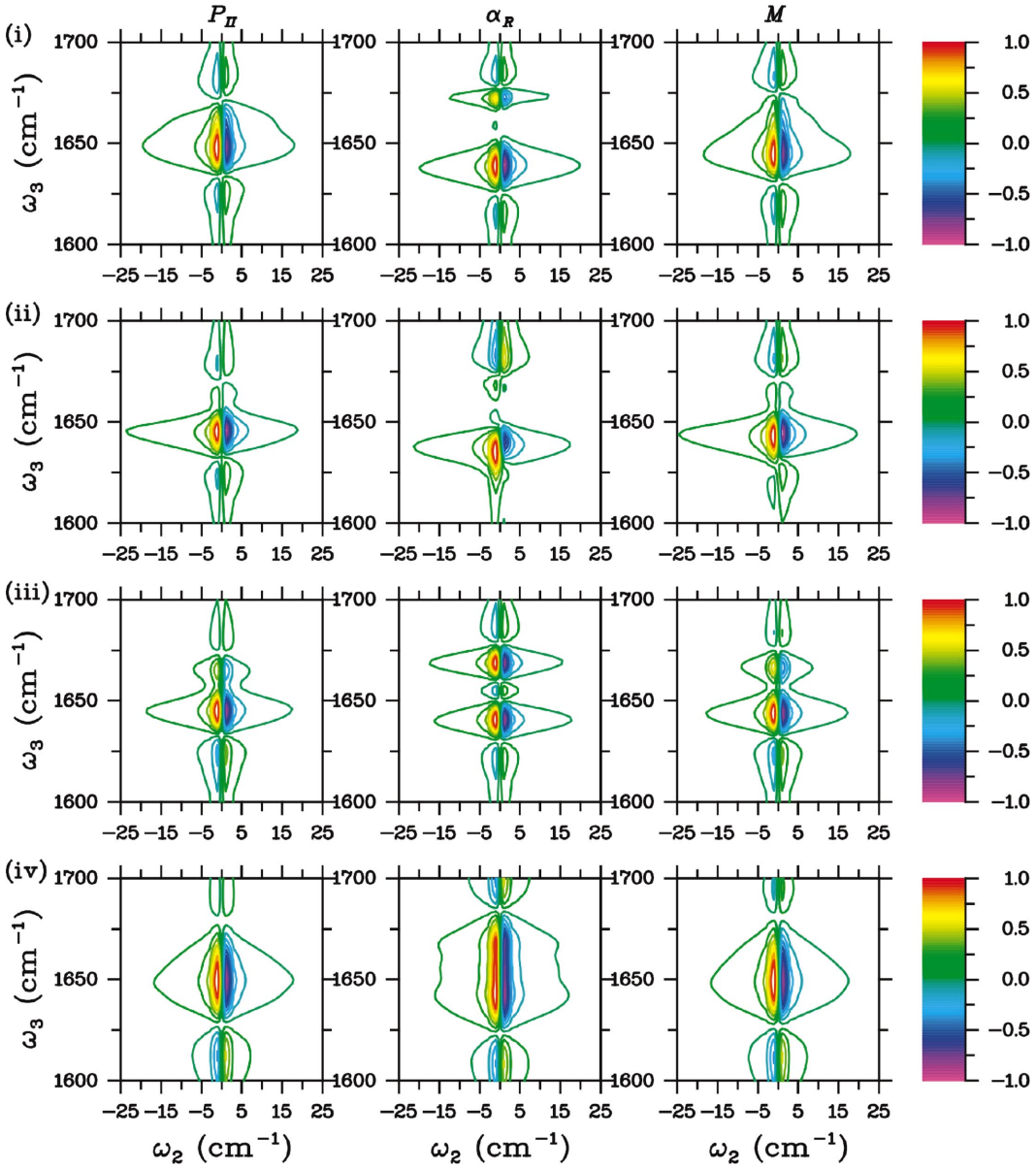

FIG. 18. (Color) Same as Fig. 15 but for S^{II}_{ZZZZ}.

we have neglected fluctuations of the anharmonicity and transition dipole moments. The stochastic variables are treated as Gaussian with the Brownian oscillator model. The distributions of the Ramachandran angles are not perfectly Gaussian, as can also be seen in Fig. 7, where the contours for the configuration distributions are not perfectly elliptical and in Fig. 8, where the Gaussian fits are shown. However, these are small deviations and the model accounts for the major part of distribution.

We therefore believe that the majority of the difference between experiment and simulations are due to the parameters obtained from the molecular dynamics simulations than deficiencies in the SLE. It is clear that accounting for the dynamics of the Ramachandran angles even within each configuration is very important. Whether this affects the spectra of larger and more rigid peptide systems still remains to be seen.

The S^{II}_{ZZZZ} and S^{II}_{ZZYY} spectra have not been measured yet. The four models give different spectra also for this technique. This means that also for this technique the fluctuations of the Ramachandran angles and the difference between a model with a fixed exciton basis and a local basis cannot be neglected. Since all peaks have ω_2 close to zero this technique does not resolve well.

The S^{III}_{ZZZZ} and S^{III}_{ZZYY} spectra show the greatest difference between the different models. Especially for the S^{III}_{ZZYY} spectrum going from model (iii) to model (ii) and introducing the fluctuations of the Ramachandran angles gave rise to a clear reduction in the number of peaks due to motional narrowing. S^{III} provides the clearest way of distinguishing between the different models and is the most sensitive of the three presented techniques.

The SLE response for one configuration was fitted to the experimental linear absorption spectrum. Good fits were obtained by either including fluctuations of the Ramachandran

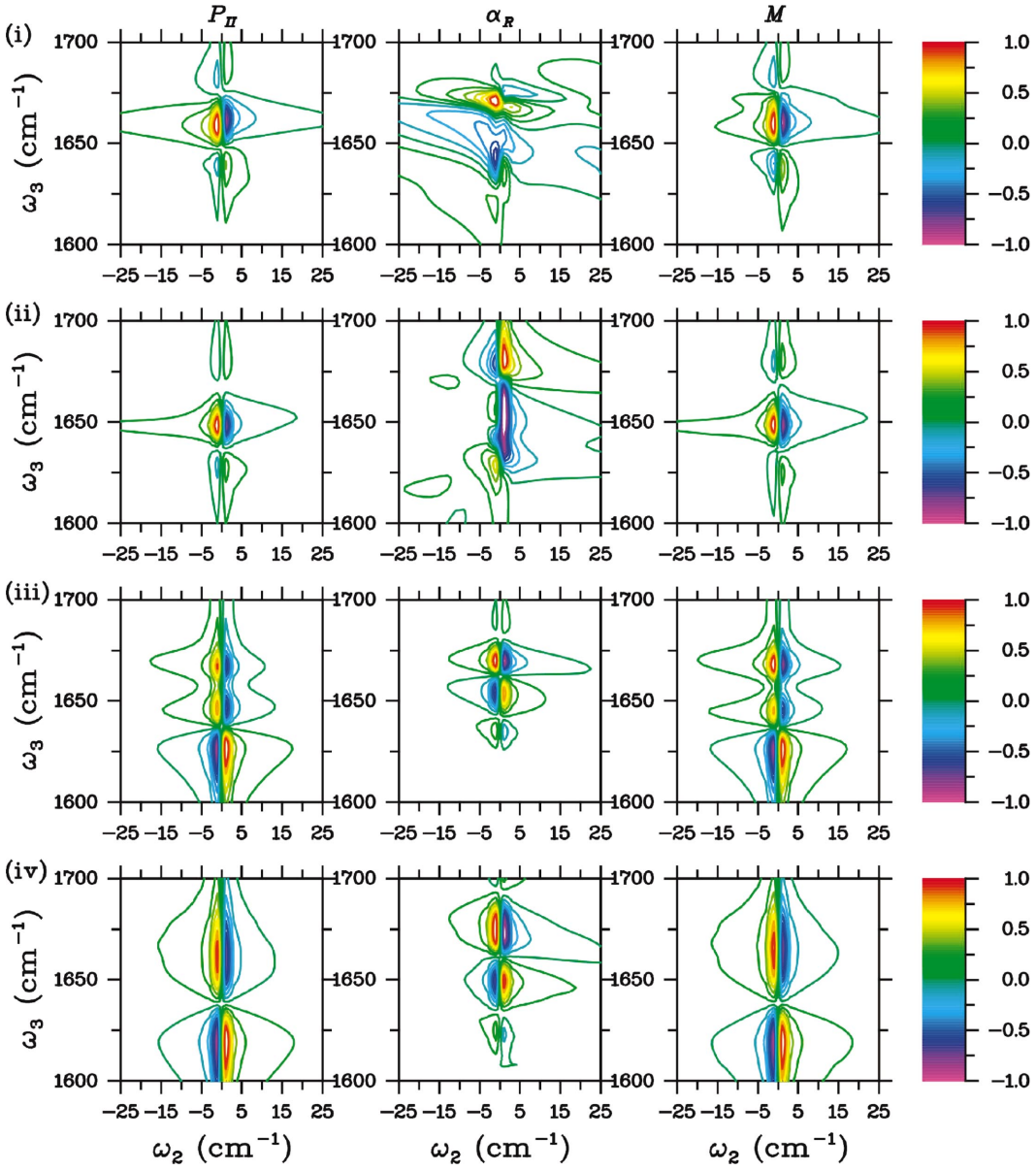

FIG. 19. (Color) Same as 15 but for S^{II}_{ZZYY}.

angles (fit A) or excluding them (fit B). The parameters were restricted to the vicinity of the those obtained by molecular dynamics simulation for P_{II}. We did not fit the 2D IR spectrum. The fitting procedure requires the calculation of numerous spectra with different values for the fitting parameters. The fits show that only one configuration is needed to reproduce the linear spectrum and that the same linear spectra can be fitted well regardless on whether the fluctuations of the Ramachandran angles are included; the linear absorption is not sensitive to Ramachandran angle fluctuations.

The linear absorption fits are not unique. The S^I spectra for the two fits are shown in Fig. 22. The S^I_{ZZZZ} spectra for the two fits are virtually identical. This spectrum is therefore not sensitive to the fluctuations of the Ramachandran angles. The S^I_{ZZYY} spectra are on the other hand very different. The negative peak is below the diagonal for fit B, while it is clearly above the diagonal for fit A. The positive overtone peaks are less sensitive. The two different fits can clearly be distinguished in this spectrum.

Distinct differences between the A and B fits are also observed in the S^{III}_{ZZZZ} and $^{III}_{ZZYY}$ spectra shown in Fig. 23. In the $ZZZZ$ spectrum fit A shows more peaks than B. The B peaks correspond to pathways involving either only the low frequency mode or the high frequency node. The extra peaks correspond to pathways involving the e_1e_2 coherence during time t_2. Similarly, more peaks are observed in the perpendicular polarized spectra going from fit B to fit A.

The fluctuations of the coupling between the two amide I oscillators were directly connected to the fluctuations of the Ramachandran angles determining the peptide structure, which in turn were obtained from molecular dynamics simulations. The fluctuations of the fundamental frequencies were not directly connected to the motion of a specific structural element. However, if a specific set of collective coordinates

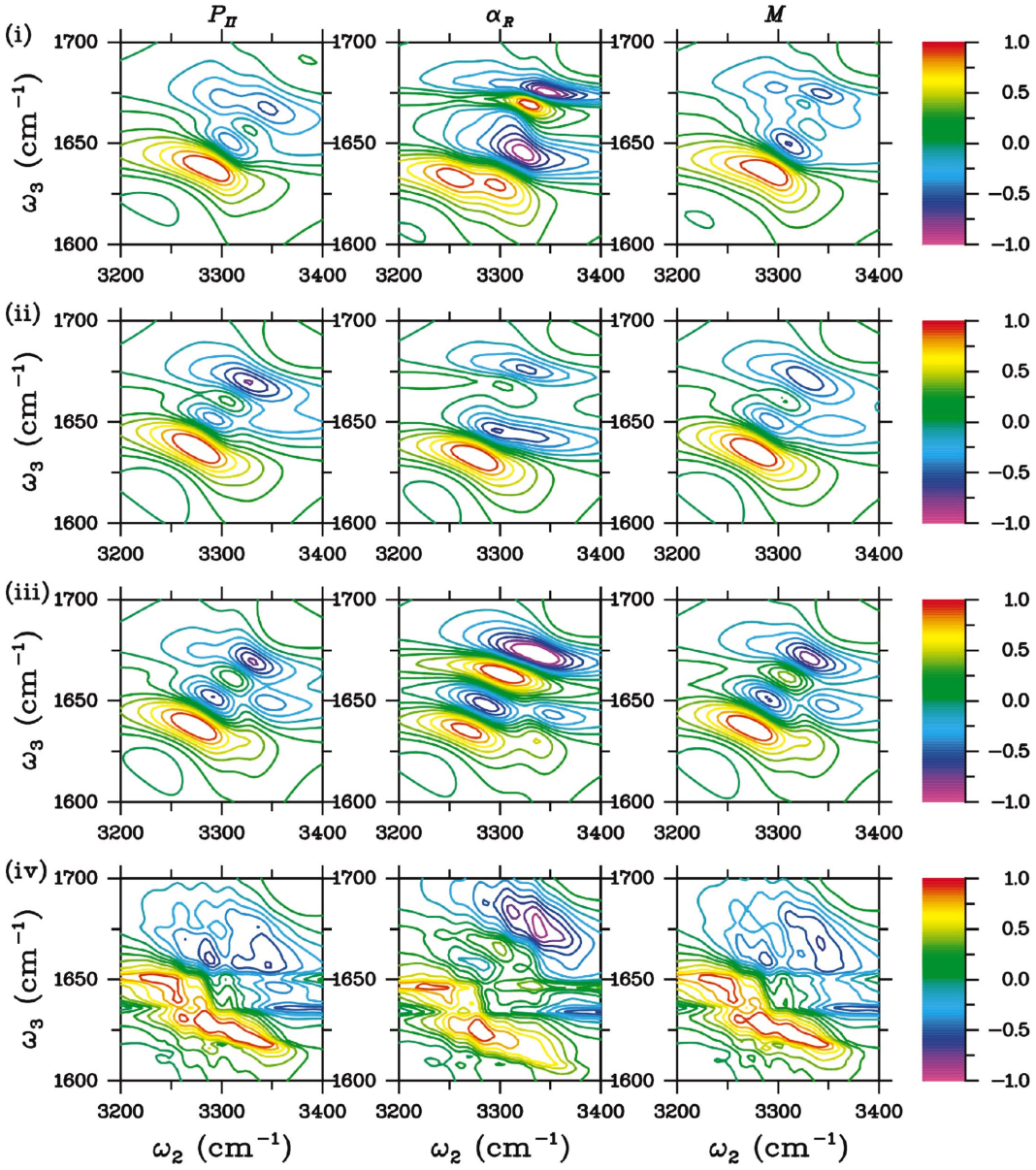

FIG. 20. (Color) Same as Fig. 15 but for S^{III}_{ZZZZ}.

responsible for these fluctuations can be identified, as for example the coordinates describing the hydrogen bonding, it should be possible to establish such a direct connection.

In summary, a stochastic Liouville equation approach for the linear and nonlinear infrared spectra accounts for the effect of the fluctuations of collective bath coordinates on the line shapes by describing the evolution for the bath and system coordinates simultaneously. At the same time the nonadiabatic coupling is accounted for. Four collective coordinates were used to account for the effect of the bath on the two amide I modes for trialanine. We showed that the fluctuations of the Ramachandran angles are important in a flexible peptide such as trialanine.

The nonadiabatic coupling between the two states arising from the fluctuations of the local mode frequencies only separated by only about 20 cm^{-1} is important both in the linear and nonlinear spectra transferring intensity between the peaks.

In the present formalism the Green's functions describing the time evolution of the collective and system coordinates are computed directly in the frequency domain. In this way the two-dimensional Fourier transforms needed in the cumulant expansion of Gaussian fluctuations CGF are avoided.[35,37]

ACKNOWLEDGMENTS

The support of the National Institutes of Health Grant No. (RO1 GM59230-04) and the National Science Foundation Grant No. (CHE-0132571) is gratefully acknowledged. We are grateful to Peter Hamm for providing the experimental data.

APPENDIX A: GREEN FUNCTION SOLUTION OF THE STOCHASTIC LIOUVILLE EQUATION

The right eigenfunction are defined as

$$\Gamma(\mathbf{\Omega})\phi_n(\mathbf{\Omega}) = \lambda_n \phi_n(\mathbf{\Omega}) \tag{A1}$$

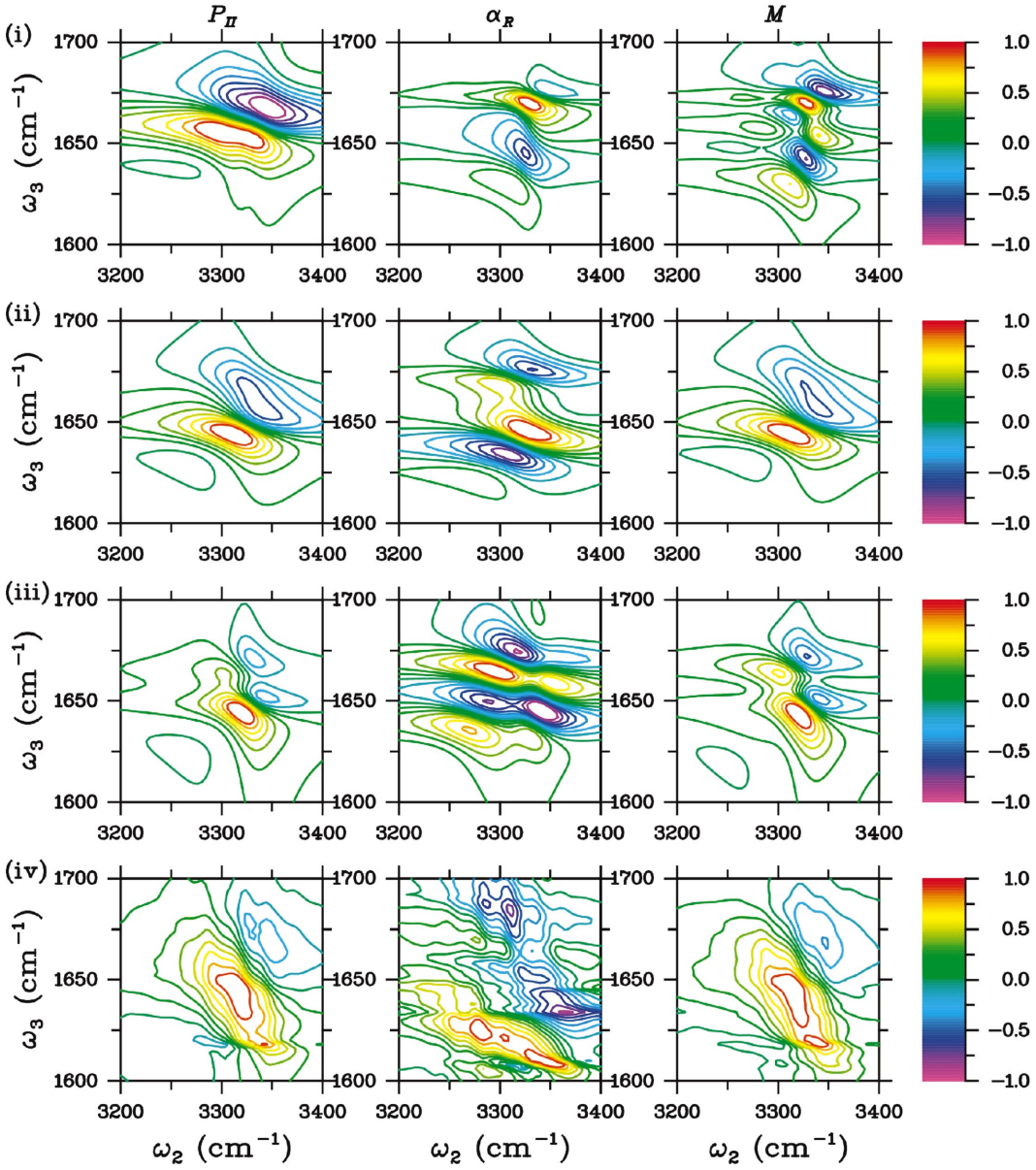

FIG. 21. (Color) Same as Fig. 15 but for S^{III}_{ZZYY}.

and the left eigenfunctions as

$$\phi'_n(\mathbf{\Omega})\Gamma(\mathbf{\Omega})=\lambda_n\phi'_n(\mathbf{\Omega}). \tag{A2}$$

The right eigenfunction with eigenvalue 0 is the equilibrium distribution according to the equilibrium condition

$$\frac{\partial P^{\mathrm{eq}}}{\partial t}=-\Gamma(\mathbf{\Omega})P^{\mathrm{eq}}(\mathbf{\Omega})=0. \tag{A3}$$

The left eigenfunction with eigenvalue 0 is the unit vector. The nth right eigenfunction has the same eigenvalue as the nth left eigenfunction. The right and left eigenfunctions are orthonormal ($\langle\phi'_n(\mathbf{\Omega})|\phi_m(\mathbf{\Omega})\rangle=\delta_{nm}$).

To solve Eq. (25) we first expand the density matrix in terms of the (right-hand) eigenfunctions of the relaxation operator:

$$\rho(\mathbf{\Omega},t)=\sum_n \mathbf{C}_n(t)\phi_n(\mathbf{\Omega}). \tag{A4}$$

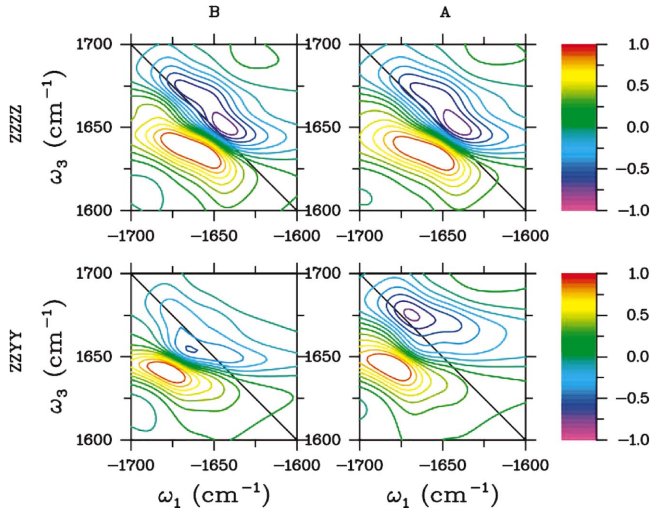

FIG. 22. (Color) S^{I}_{ZZZZ} spectra (upper row) and S^{I}_{ZZYY} (lower row) for the two fits. Models A (right column) and B (left column).

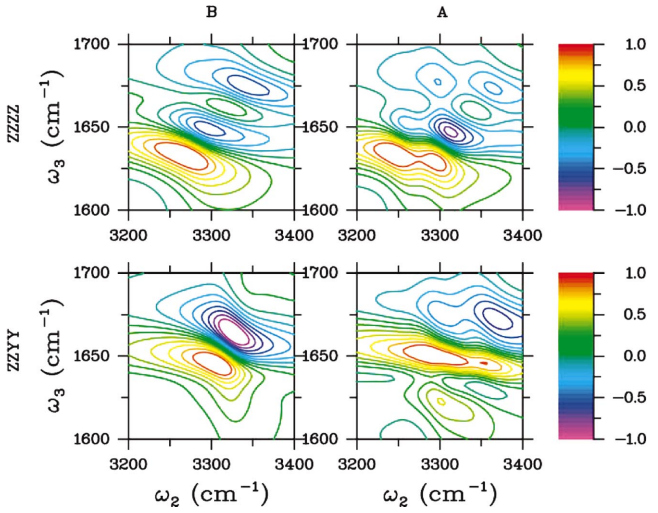

FIG. 23. (Color) S^{III}_{ZZZZ} spectra (upper row) and S^{III}_{ZZYY} (lower row) for the two fit models A (right column) and B (left column).

Insetting the expansion of Eq. (A4) into the SLE [Eq. (25)] gives

$$\sum_n \dot{\mathbf{C}}_n(t)\phi_n(\mathbf{\Omega}) = \sum_m \left[-\frac{i}{\hbar}\mathbf{L}(\Omega)\mathbf{C}_m(t)\phi_m(\mathbf{\Omega}) - \Gamma(\mathbf{\Omega})\mathbf{C}_m(t)\phi_m(\mathbf{\Omega}) \right]. \tag{A5}$$

Using that $\phi_m(\mathbf{\Omega})$ is a right eigenfunction of $\Gamma(\mathbf{\Omega})$, multiplying with a left eigenfunction $\phi_m(\mathbf{\Omega})$, and integrating over $\mathbf{\Omega}$ the equation becomes

$$\sum_n \dot{\mathbf{C}}_n(t)\langle\phi'_k(\mathbf{\Omega})|\phi_n(\mathbf{\Omega})\rangle = \sum_m \left[-\frac{i}{\hbar}\langle\phi'_k(\mathbf{\Omega})|\mathbf{L}(\Omega)|\phi_m(\mathbf{\Omega})\rangle\mathbf{C}_m(t) - \lambda_m\mathbf{C}_m(t) \times\langle\phi'_k(\mathbf{\Omega})|\phi_m(\mathbf{\Omega})\rangle \right]. \tag{A6}$$

Using the orthonormality of the eigenfunctions leads to the final equation

$$\dot{\mathbf{C}}_k(t) = -\lambda_k\mathbf{C}_k(t) - \frac{i}{\hbar}\sum_m \langle\phi'_k(\mathbf{\Omega})|\mathbf{L}(\Omega)|\phi_m(\mathbf{\Omega})\rangle\mathbf{C}_m(t). \tag{A7}$$

The matrix elements $\langle\phi'_k(\mathbf{\Omega})|\mathbf{L}(\Omega)|\phi_m(\mathbf{\Omega})\rangle$ depend on both the relaxation operator and on how the Liouville operator depend on the stochastical bath variables $\mathbf{\Omega}$. The formal Green's function solution to Eq. (A7) is

$$\mathbf{C}_n(t) = \sum_{m=0}^{\infty} \mathbf{G}_{n,m}(t)\mathbf{C}_m(0). \tag{A8}$$

The matrices $\mathbf{C}_n(t)$ can be found from the coefficients at earlier times by numerical integration of Eq. (A7), when the eigenfunction expansion is truncated at an appropriate level.

The system density matrix is then found by tracing over the bath coordinates

$$\boldsymbol{\rho}(t) = \int \boldsymbol{\rho}(\mathbf{\Omega},t)d\mathbf{\Omega} = \int \sum_n \mathbf{C}_n(t)\phi_n(\mathbf{\Omega})d\mathbf{\Omega} = \sum_n \mathbf{C}_n(t)\langle\phi_0(\mathbf{\Omega})|\phi_n(\mathbf{\Omega})\rangle = \mathbf{C}_0(t). \tag{A9}$$

The Green's function operator in the joint system and bath space is denoted $\mathcal{G}(\mathbf{\Omega}',\mathbf{\Omega},t)$ with matrix elements $G^{ab,cd}_{i,j}(t)$, where i and j relate to the bath and ab and cd to the system in Liouville space. The bath space matrix element of $\mathcal{G}(\mathbf{\Omega}',\mathbf{\Omega},t)$ is denoted $\mathbf{G}_{n,m}(t)$ and is operating on the system coordinates only. The system space matrix element of $\mathcal{G}(\mathbf{\Omega}',\mathbf{\Omega},t)$ is denoted $\mathcal{G}^{ab,cd}(\Omega',\Omega,t)$.

The linear and nonlinear responses can be obtained from the Green's functions as shown in Appendix B. The Green's functions are calculated numerically in frequency domain using the continued fraction[51] as described in Appendix E.

APPENDIX B: THE LINEAR AND THE THIRD-ORDER RESPONSE

The linear spectrum is determined by the time evolution of density matrix elements ρ_{eg}, where e denotes an excited state and g the ground state. For the linear response the bath initially has the equilibrium distribution and $\mathbf{C}_n(t)$ is zero for $n>0$. The trace of the density matrix at time t only depends on $\mathbf{C}_0(t)$. Therefore we only need to find $\mathbf{G}_{0,0}(t)$. The linear response in time domain is

$$S^{(1)}(t) = \mathrm{Re}\left(\frac{i}{\hbar}\sum_{a,b}\mu_{gb}G^{bg,ag}_{0,0}(t)\mu_{ag}\right), \tag{B1}$$

where μ_{gb} is the transition dipole from the excited state b to the ground state g. $G^{bg,ag}_{0,0}(t)$ is a matrix element of the Green's function $\mathbf{G}_{0,0}(t)$. This Green's function is the upper left matrix element of the Green's function matrix $\mathcal{G}_{0,0}(t)$.

The third-order response is given by the sum of four Liouville space pathways. (and their complex conjugates):

$$S^{(3)}(t_3,t_2,t_1) = \left(\frac{i}{\hbar}\right)^3\sum_i^4 [R_i(t_3,t_2,t_1) - R_i^*(t_3,t_2,t_1)]. \tag{B2}$$

A Fourier transform is often performed of the time variables t_1 and t_3 giving the frequency domain variables ω_1 and ω_3. A Fourier transform of the time variable t_2 gives the frequency domain variable ω_2.

In the SLE formulation the first Liouville pathway is given by

$$R_1(\omega_3,\omega_2,\omega_1) = \int\int\int\int \sum_{abcdefghjk} \mu^{kk,jk}(\mathbf{\Omega}''') \times G^{jk,fh}(\mathbf{\Omega}''',\mathbf{\Omega}'',\omega_3)\mu^{fh,fg}(\mathbf{\Omega}'') \times G^{fg,de}(\mathbf{\Omega}'',\mathbf{\Omega}',\omega_2)\mu^{de,dc}(\mathbf{\Omega}') \times G^{dc,ba}(\mathbf{\Omega}',\mathbf{\Omega},\omega_1)\mu^{ba,aa}(\mathbf{\Omega}) \times W(\mathbf{\Omega})P(a)d\mathbf{\Omega}'''\,d\mathbf{\Omega}''\,d\mathbf{\Omega}'\,d\mathbf{\Omega}, \tag{B3}$$

where $W(\mathbf{\Omega})$ is the equilibrium distribution of the bath coordinates. $P(a)$ is the population of quantum state a. Introducing a shorthand notation, where $\langle\cdots\rangle$ denotes the integrations over the bath coordinates and the sums over quantum states this can be written as

$$R_1(\omega_3,\omega_2,\omega_1)=\langle\hat{\mu}^{kk,jk}\hat{G}^{jk,fh}(\omega_3)\hat{\mu}^{fh,fg}\hat{G}^{fg,de}(\omega_2)\times\hat{\mu}^{de,dc}\hat{G}^{dc,ba}(\omega_1)\hat{\mu}^{ba,aa}\rangle. \tag{B4}$$

The remaining three of the four independent Liouville space pathways are in this notation

$$R_2(\omega_3,\omega_2,\omega_1)=\langle\hat{\mu}^{kk,jk}\hat{G}^{jk,fh}(\omega_3)\hat{\mu}^{fh,fg}\hat{G}^{fg,ed}(\omega_2)\times\hat{\mu}^{ed,cd}\hat{G}^{cd,ab}(\omega_1)\hat{\mu}^{ab,aa}\rangle, \tag{B5}$$

$$R_3(\omega_3,\omega_2,\omega_1)=\langle\hat{\mu}^{kk,jk}\hat{G}^{jk,hf}(\omega_3)\hat{\mu}^{hf,gf}\hat{G}^{gf,de}(\omega_2)\times\hat{\mu}^{de,dc}\hat{G}^{dc,ab}(\omega_1)\hat{\mu}^{ab,aa}\rangle, \tag{B6}$$

$$R_4(\omega_3,\omega_2,\omega_1)=\langle\hat{\mu}^{kk,jk}\hat{G}^{jk,hf}(\omega_3)\hat{\mu}^{hf,gf}\hat{G}^{gf,ed}(\omega_2)\times\hat{\mu}^{ed,cd}\hat{G}^{cd,ba}(\omega_1)\hat{\mu}^{ba,aa}\rangle. \tag{B7}$$

Using the Green's function matrices $\mathcal{G}(\omega)$ and transition dipole matrices $\mathcal{M}$, with the matrix elements in the basis of the eigenfunctions of $\Gamma(\mathbf{\Omega})$ defined as

$$\mathcal{M}_{ij}^{ab,cd}=\int\phi_i'(\mathbf{\Omega})\mu^{ab,cd}(\mathbf{\Omega})\phi_j(\mathbf{\Omega})d\mathbf{\Omega}, \tag{B8}$$

the response functions can be recast as

$$R_1(\omega_3,\omega_2,\omega_1)=\sum_{abcdefghjk}[\mathcal{M}^{kk,jk}\mathcal{G}^{jk,fh}(\omega_3)\times\mathcal{M}^{fh,fg}\mathcal{G}^{fg,de}(\omega_2)\times\mathcal{M}^{de,dc}\mathcal{G}^{dc,ba}(\omega_1)\mathcal{M}^{ba,aa}]_{00}P(a), \tag{B9}$$

$$R_2(\omega_3,\omega_2,\omega_1)=\sum_{abcdefghjk}[\mathcal{M}^{kk,jk}\mathcal{G}^{jk,fh}(\omega_3)\times\mathcal{M}^{fh,fg}\mathcal{G}^{fg,ed}(\omega_2)\times\mathcal{M}^{ed,cd}\mathcal{G}^{cd,ab}(\omega_1)\mathcal{M}^{ab,aa}]_{00}P(a), \tag{B10}$$

$$R_3(\omega_3,\omega_2,\omega_1)=\sum_{abcdefghjk}[\mathcal{M}^{kk,jk}\mathcal{G}^{jk,fh}(\omega_3)\times\mathcal{M}^{hf,gf}\mathcal{G}^{gf,de}(\omega_2)\times\mathcal{M}^{de,dc}\mathcal{G}^{dc,ab}(\omega_1)\mathcal{M}^{ab,aa}]_{00}P(a), \tag{B11}$$

$$R_4(\omega_3,\omega_2,\omega_1)=\sum_{abcdefghjk}[\mathcal{M}^{kk,jk}\mathcal{G}^{jk,fh}(\omega_3)\times\mathcal{M}^{hf,gf}\mathcal{G}^{gf,ed}(\omega_2)\times\mathcal{M}^{ed,cd}\mathcal{G}^{cd,ba}(\omega_1)\mathcal{M}^{ba,aa}]_{00}P(a). \tag{B12}$$

Here $[\cdots]_{00}$ denote the 00 matrix element of the matrix product in the bath space. The Green's function matrices $\mathcal{G}$ are calculated using the continued fraction as described in chapter 9 of Ref. 51. The transition dipole matrix elements are evaluated by expanding the transition dipole operators $\mu^{ab,cd}(\mathbf{\Omega})$ in the bath coordinates $\mathbf{\Omega}$ and evaluating the matrix elements using Eq. (B8).

When considering a specific experiment like the photon echo some of the Liouville space pathways are forbidden by the rotating wave approximation[52] and will not contribute to the spectrum. In the photon echo experiment, the Liouville space pathways corresponding to the Feynman diagrams in Fig. 4 are the only ones contributing. When the Hamiltonian is not coupling different excitation manifolds as the Hamiltonian used here [Eq. (1)], the Green's functions contributing for a specific time interval can be characterized by the density matrix blocks of which they describe the evolution as described in Sec. III. Denoting states by the number of excitations they have e and an index i as e_i one can keep track of the excitation manifolds. Using this notation a Green's function matrix describing the time evolution of each of the density matrix blocks described in Sec. III can be constructed independently. The Green's function matrix governing the time evolution of the density matrix block ρ^{eg} is denoted $\mathcal{G}^{eg,eg}(\omega)$. In a similar way the time evolution of the first density matrix block ρ_{gg} is described by the Green's function matrix $\mathcal{G}^{gg,gg}(\omega)$. The time evolution of the third density matrix block ρ^{ee} is described by the Green's function matrix $\mathcal{G}^{ee,ee}(\omega)$. The fourth density matrix element block ρ_{fg} is described by the Green's function matrix $\mathcal{G}^{fg,fg}(\omega)$. The Green's function matrix $\mathcal{G}^{fe,fe}(\omega)$ describes the time evolution of the fifth density matrix block ρ_{fe}.

Using this notation to keep track of the numbers of excitations the three Liouville space pathways contributing to the photon echo signal are then written as

$$S^I(\omega_3,\omega_2,\omega_1)=\left(\frac{i}{\hbar}\right)^3[R_2(\omega_3,\omega_2,\omega_1)+R_3(\omega_3,\omega_2,\omega_1)-R_1^*(\omega_3,\omega_2,\omega_1)], \tag{B13}$$

where

$$R_2(\omega_3,\omega_2,\omega_1)=[\mathcal{M}^{gg,eg}\mathcal{G}^{eg,eg}(\omega_3)\mathcal{M}^{eg,ee}\mathcal{G}^{ee,ee}(\omega_2)\times\mathcal{M}^{ee,ge}\mathcal{G}^{ge,ge}(\omega_1)\mathcal{M}^{ge,gg}]_{00}, \tag{B14}$$

$$R_3(\omega_3,\omega_2,\omega_1)=[\mathcal{M}^{gg,eg}\mathcal{G}^{eg,eg}(\omega_3)\mathcal{M}^{eg,gg}\times\mathcal{G}^{gg,gg}(\omega_2)\mathcal{M}^{gg,ge}\mathcal{G}^{ge,ge}(\omega_1)\times\mathcal{M}^{ge,gg}]_{00}, \tag{B15}$$

$$R_1^*(\omega_3,\omega_2,\omega_1)=[\mathcal{M}^{ee,fe}\mathcal{G}^{fe,fe}(\omega_3)\mathcal{M}^{fe,ee}\mathcal{G}^{ee,ee}(\omega_2)\times\mathcal{M}^{ee,ge}\mathcal{G}^{ge,ge}(\omega_1)\mathcal{M}^{ge,gg}]_{00}. \tag{B16}$$

This expression allows utilizing the block diagonal structure of the density matrix and thereby the overall Green's function.

To obtain the 2D IR spectrum the frequency ω_2 need to be transformed to the time domain. Alternatively the Green's function involving t_2 can be evaluated directly in time domain by integration of the SLE. In the special case, where t_2 is zero the Green's function $\mathcal{G}(t_2)$ is a unit matrix. The Green's function matrix $\mathcal{G}(\omega_2)$ can in this case simply be ignored.

For the $\mathbf{k}_{II}$ technique the response is determined by the Liouville space pathways (see Fig. 5)

$$S^{II}(\omega_3,\omega_2,\omega_1)=\left(\frac{i}{\hbar}\right)^3[R_1(\omega_3,\omega_2,\omega_1)+R_4(\omega_3,\omega_2,\omega_1)-R_2^*(\omega_3,\omega_2,\omega_1)], \tag{B17}$$

$$R_1(\omega_3,\omega_2,\omega_1)=[\mathcal{M}^{gg,eg}\mathcal{G}^{eg,eg}(\omega_3)\mathcal{M}^{eg,ee}\mathcal{G}^{ee,ee}(\omega_2)\times\mathcal{M}^{ee,eg}\mathcal{G}^{eg,eg}(\omega_1)\mathcal{M}^{eg,gg}]_{00}, \tag{B18}$$

$$R_4(\omega_3,\omega_2,\omega_1)=[\mathcal{M}^{gg,eg}\mathcal{G}^{eg,eg}(\omega_3)\mathcal{M}^{eg,gg}\mathcal{G}^{gg,gg}(\omega_2)\times\mathcal{M}^{gg,eg}\mathcal{G}^{eg,eg}(\omega_1)\mathcal{M}^{eg,gg}]_{00}, \tag{B19}$$

$$R_2^*(\omega_3,\omega_2,\omega_1)=[\mathcal{M}^{ee,fe}\mathcal{G}^{fe,fe}(\omega_3)\mathcal{M}^{fe,ee}\mathcal{G}^{ee,ee}(\omega_2)\times\mathcal{M}^{ee,eg}\mathcal{G}^{eg,eg}(\omega_1)\mathcal{M}^{eg,gg}]_{00}. \tag{B20}$$

For the calculations of the $\mathbf{k}_{II}$ spectra the time delay t_1 was kept fixed and the Green's function $\mathcal{G}(\omega_1)$ was ignored analogous to what was done for the photon echo spectrum.

For the $\mathbf{k}_{III}$ technique the response is determined by two Liouville space pathways (see Fig. 6)

$$S^{III}(\omega_3,\omega_2,\omega_1)=\left(\frac{i}{\hbar}\right)^3[R_4(\omega_3,\omega_2,\omega_1)-R_3^*(\omega_3,\omega_2,\omega_1)], \tag{B21}$$

$$R_4(\omega_3,\omega_2,\omega_1)=[\mathcal{M}^{gg,eg}\mathcal{G}^{eg,eg}(\omega_3)\mathcal{M}^{eg,fg}\mathcal{G}^{fg,fg}(\omega_2)\times\mathcal{M}^{fg,eg}\mathcal{G}^{eg,eg}(\omega_1)\mathcal{M}^{eg,gg}]_{00}, \tag{B22}$$

$$R_3^*(\omega_3,\omega_2,\omega_1)=[\mathcal{M}^{ee,fe}\mathcal{G}^{fe,fe}(\omega_3)\mathcal{M}^{fe,fg}\mathcal{G}^{fg,fg}(\omega_2)\times\mathcal{M}^{fg,eg}\mathcal{G}^{eg,eg}(\omega_1)\mathcal{M}^{eg,gg}]_{00}. \tag{B23}$$

For the calculations of the $\mathbf{k}_{III}$ spectra the time delay t_1 was kept fixed.

APPENDIX C: THE BROWNIAN OSCILLATOR

The relaxation operator for the Brownian oscillator is given by the Smoluchowski equation[39]

$$\Gamma(\Omega)=\gamma\frac{\partial}{\partial\Omega}\left(\Delta^2\frac{\partial}{\partial\Omega}+\Omega\right). \tag{C1}$$

The right eigenfunctions are

$$\phi_n(\Omega)=\frac{1}{2^n\sqrt{2\pi}n!\Delta}\exp\left(-\frac{\Omega^2}{2\Delta^2}\right)H_n\left(\frac{\Omega}{\Delta\sqrt{2}}\right), \tag{C2}$$

and the left eigenfunctions are

$$\phi_n'(\Omega)=H_n\left(\frac{\Omega}{\Delta\sqrt{2}}\right). \tag{C3}$$

$H_n(x)$ are Hermite polynomials fulfilling the recurrence relation

$$H_{n+1}(x)=2xH_n(x)-2nH_{n-1}(x). \tag{C4}$$

The eigenvalues are $n\gamma$. From the recurrence relation the following integrals needed in order to calculate the matrix elements of $\mathbf{L}(\Omega)$ can be evaluated

$$\begin{aligned}
&\langle\phi_n'(\Omega)|\phi_m(\Omega)\rangle=\delta_{m,n}\\
&\langle\phi_n'(\Omega)|\Omega|\phi_m(\Omega)\rangle=\Delta\sqrt{2}[\delta_{m,n+1}/2+n\delta_{m,n-1}]\\
&\langle\phi_n'(\Omega)|\Omega^2|\phi_m(\Omega)\rangle=2\Delta^2[\delta_{m,n+2}/4+(n+1/2)\delta_{m,n}+n(n-1)\delta_{m,n-2}].
\end{aligned} \tag{C5}$$

APPENDIX D: THE RESPONSE IN THE ADIABATIC REPRESENTATION

The expansion in the dynamic basis [Eq. (6)] is substituted into the time dependent Schrödinger equation in order to obtain the time evolution of the expansion coefficients $c_i(t)$:

$$\sum_i\left(\frac{\partial[c_i(t)|\tilde{\psi}_i(t)\rangle]}{\partial t}\right)=-\frac{i}{\hbar}\sum_i c_i(t)H(t)|\tilde{\psi}_i(t)\rangle. \tag{D1}$$

The derivative of the product on the left side is taken and on the right side the fact that $\psi_i(t)$ is the eigenfunction of $H(t)$ with the eigenvalue $\epsilon_i(t)$ is used. A dot denotes a time derivative:

$$\sum_i|\dot{\psi}_i(t)\rangle c_i(t)+\sum_i\dot{c}_i(t)|\tilde{\psi}_i(t)\rangle)=-\frac{i}{\hbar}\sum_i c_i(t)\epsilon_i(t)|\tilde{\psi}_i(t)\rangle. \tag{D2}$$

The first term on the left-hand side is moved to the right-hand side and the equation is multiplied with one of the eigenfunctions $\psi_j(t)$ from the left:

$$\sum_i\dot{c}_i(t)\langle\tilde{\psi}_j(t)|\tilde{\psi}_i(t)\rangle=-\frac{i}{\hbar}\sum_i c_i(t)\epsilon_i(t)\langle\tilde{\psi}_j(t)|\tilde{\psi}_i(t)\rangle-\sum_i\langle\tilde{\psi}_j(t)|\dot{\tilde{\psi}}_i(t)\rangle c_i(t). \tag{D3}$$

This leads to the final expression for the time evolution of the expansion coefficients in the adiabatic basis

$$\dot{c}_j(t)=-\frac{i}{\hbar}c_j(t)\epsilon_j(t)-\sum_i\langle\tilde{\psi}_j(t)|\dot{\tilde{\psi}}_i(t)\rangle c_i(t). \tag{D4}$$

Defining the matrix K,

$$K_{jk}(t)\equiv\epsilon_j(t)\delta_{jk}-i\hbar S_{jk}(t), \tag{D5}$$

the general solution to Eq. (7) can be written in matrix form assuming that the vector of expansion coefficients c are known at some time t_0:

$$c(t)\equiv U^c(t,t_0)c(t_0)=\exp_+\left[-\int_{t_0}^t\frac{i}{\hbar}K(t')dt'\right]c(t_0). \tag{D6}$$

U^c which describes the time evolution of the expansion coefficients depends on the nonadiabatic coupling matrix S and the diagonal eigenvalue matrix $\boldsymbol{\epsilon}$. $\exp_+$ is the time ordered exponential.[52]

The time evolution of the wave function in the adiabatic representation is

$$|\phi(\tau_1)\rangle = \sum_{ab} |\tilde{\psi}_a(\tau_1)\rangle \left[\exp_+ \left(-\int_{\tau_0}^{\tau_1} \frac{i}{\hbar} K(\tau) d\tau \right) \right]_{ab} \times \langle \tilde{\psi}_b(\tau_0) | \phi(\tau_0) \rangle. \tag{D7}$$

Generally this is not easier to evaluate than in a fixed basis. It still involves a time ordered exponential of a time dependent matrix with N^2 elements, where N is the number of relevant eigenfunctions and expansion coefficients. However, if the nonadiabatic coupling is negligible or only involves a few eigenstates the time evolution can be simplified considerably.

If the time variation of the adiabatic basis function is slow ($|\dot{\phi}_c(\tau)\rangle \approx 0$) the nonadiabatic coupling can be neglected. This *adiabatic approximation* will break down, when the instantaneous eigenvalues cross. When the nonadiabatic coupling is neglected the time evolution operator becomes diagonal and each expansion coefficient in Eq. (D6) evolves independently of the others. This allows us to follow the time evolution of each adiabatic state separately.

If the nonadiabatic coupling is negligible only the diagonal $\boldsymbol{\epsilon}(t')$ matrix is left over in Eq. (D6) and the evolution of each expansion coefficient is independent of the others. In this adiabatic approximation the time evolution of the expansion coefficients is simply

$$c_j(\tau_1) = \exp\left[-\int_{\tau_0}^{\tau_1} \frac{i}{\hbar} \epsilon_j(\tau') d\tau' \right] c_j(\tau_0) \equiv I_j(\tau_{10}) c_j(\tau_0), \tag{D8}$$

which means that each expansion coefficient simply acquire a phase $[I_j(\tau_{10})]$ as time evolves.

The time dependent wave function in the adiabatic approximation is

$$|\phi(\tau_1)\rangle = \left[\sum_j |\tilde{\psi}_j(\tau_1)\rangle \times \exp\left(-\frac{i}{\hbar} \int_{\tau_0}^{\tau_1} \epsilon_j(\tau) d\tau \right) \langle \tilde{\psi}_j(\tau_0)| \right] |\phi(\tau_0)\rangle \equiv U(\tau_{10}) |\phi(\tau_0)\rangle. \tag{D9}$$

In the adiabatic representation, the linear response is

$$S^{(1)}(t_1) = \frac{i}{\hbar} \sum_{abcd} \mu_{dc}(t_1) U^c_{cb}(t_1) \mu_{ba}(0) U^{c\dagger}_{da}(t_1) P(a) + \text{c.c.} \tag{D10}$$

When the adiabatic approximation is evoked the expression simplifies to

$$S^{(1)}(t_1) = \frac{i}{\hbar} \sum_{ab} \mu_{ab}(t_1) U_{bb}(t_1) \mu_{ba}(0) U^{\dagger}_{aa}(t_1) P(a) + \text{c.c.} \tag{D11}$$

The four point correlation function in Eq. (9) determining the nonlinear response is in the adiabatic basis given by

$$\begin{aligned} &\langle \mu(\tau_1)\mu(\tau_2)\mu(\tau_3)\mu(\tau_4) \rangle \\ &= \sum_{a\cdots m} \langle \phi(\tau_0)|\tilde{\psi}_a(\tau_0)\rangle \langle \tilde{\psi}_m(\tau_0)|\phi(\tau_0)\rangle U^{c\dagger}_{al}(\tau_{10}) \mu_{lk}(\tau_1) \\ &\quad \times U^c_{kj}(\tau_{10}) U^{c\dagger}_{ji}(\tau_{20}) \mu_{ih}(\tau_2) U^c_{hg}(\tau_{20}) U^{c\dagger}_{gf}(\tau_{30}) \mu_{fe}(\tau_3) \\ &\quad \times U^c_{ed}(\tau_{30}) U^{c\dagger}_{dc}(\tau_{40}) \mu_{cb}(\tau_4) U^c_{bm}(\tau_{40}). \end{aligned} \tag{D12}$$

The probability [P(a)] of being in state (a) at time τ_0 is determined by the Boltzmann distribution. The four time correlation function can then be recast as

$$\begin{aligned} &\langle \mu(\tau_1)\mu(\tau_2)\mu(\tau_3)\mu(\tau_4) \rangle \\ &= \sum_{a\cdots h} P(a) \mu_{hg}(\tau_1) U^c_{gf}(\tau_{12}) \mu_{fe}(\tau_2) U^c_{ed}(\tau_{23}) \mu_{dc}(\tau_3) \\ &\quad \times U^c_{cb}(\tau_{34}) \mu_{ba}(\tau_4) U^c_{ah}(\tau_{41}). \end{aligned} \tag{D13}$$

This general expression including the nonadiabatic coupling has eight summation indices in contrast to the less computationally demanding adiabatic approximation expression in Eq. (9) with only four summation indices. It should be noted that for the summations both in Eqs. (9) and (D12) the matrix nature of the expressions can be utilized allowing more efficient computation, when the associative law is employed. This expression for the four time correlation function in the adiabatic representation is computationally just as expensive as in a fixed basis and when the adiabatic approximation is not made the adiabatic representation need not be used.

APPENDIX E: MATRIX CONTINUED FRACTION SOLUTION OF THE SLE

The stochastic Liouville equation as given in Eq. (A7) can be solved in frequency domain using a matrix continued fraction. Following chapter 9 of Risken[51] the general recurrence relation with L nearest neighbor coupling

$$\dot{\mathbf{C}}_n(t) = \sum_{l=-L}^{L} A^l_n \mathbf{C}_{n+l}(t) \tag{E1}$$

can be cast into a tridiagonal vector recurrence relation

$$\dot{\mathcal{C}}_n(t) = \mathcal{Q}^-_n \mathcal{C}_{n-1}(t) + \mathcal{Q}_n + \mathcal{Q}^+_n \mathcal{C}_{n+1}(t). \tag{E2}$$

$\mathcal{C}_n(t)$ is a L component vector of matrices $\mathbf{C}_m(t)$:

$$\mathcal{C}_n(t) = \begin{pmatrix} \mathbf{C}_{Ln}(t) \\ \mathbf{C}_{Ln+1}(t) \\ \vdots \\ \mathbf{C}_{Ln+L-1}(t) \end{pmatrix}. \tag{E3}$$

The matrices $\mathcal{Q}^-_n$, $\mathcal{Q}_n$, and $\mathcal{Q}^+_n$ are defined by their matrix elements

$$[\mathcal{Q}^{\pm}_n]_{qr} = A^{r-q\pm L}_{Ln+q-1}, \tag{E4}$$

$$[\mathcal{Q}_n]_{qr} = A^{r-q}_{Ln+q-1}, \tag{E5}$$

setting $A^l_n = 0$ for $|l| > L$. This allows solving the general equation using the solution of the tridiagonal vector recurrence relation, i.e., Eq. (E2). In Eq. (A7) $\langle \phi'_k(\mathbf{\Omega}) | \mathbf{L}(\mathbf{\Omega}) | \phi_m(\mathbf{\Omega}) \rangle = A^{k-m}_m$.

The general solution of Eq. (E2) can be expressed in terms of the Green's function matrix $\mathcal{G}_{n,m}(t)$:

$$\mathcal{C}_n(t) = \sum_{m=0}^{\infty} \mathcal{G}_{n,m}(t)\mathcal{C}_m(0). \tag{E6}$$

The initial value is $\mathcal{G}_{n,m}(0) = \mathcal{I}\delta_{nm}$, where $\mathcal{I}$ is the unit matrix. Using this identity and taking the Laplace transform

$$\tilde{\mathcal{G}}_{n,m}(s) = \int_0^{\infty} \exp(-st)\mathcal{G}_{n,m}(t)dt \tag{E7}$$

leads to the equation

$$s\tilde{\mathcal{G}}_{n,m}(s) - \mathcal{I}\delta_{nm} = \mathcal{Q}_n^- \tilde{\mathcal{G}}_{n-1,m}(s) + \mathcal{Q}_n \tilde{\mathcal{G}}_{n,m}(s) + \mathcal{Q}_n^+ \tilde{\mathcal{G}}_{n+1,m}(s). \tag{E8}$$

Defining $\hat{\mathcal{Q}}_n = \mathcal{Q}_n - s\mathcal{I}$ gives

$$-\mathcal{I}\delta_{nm} = \mathcal{Q}_n^- \tilde{\mathcal{G}}_{n-1,m}(s) + \hat{\mathcal{Q}}_n \tilde{\mathcal{G}}_{n,m}(s) + \mathcal{Q}_n^- \tilde{\mathcal{G}}_{n+1,m}(s). \tag{E9}$$

Matrices connecting neighboring Green's functions are introduced:

$$\tilde{\mathcal{G}}_{n\pm1,m}(s) = \tilde{\mathcal{S}}^{\pm}_n(s)\tilde{\mathcal{G}}_{n,m}(s). \tag{E10}$$

When $n \neq m$ this allow writing Eq. (E9) as

$$\mathcal{Q}_n^- \tilde{\mathcal{G}}_{n-1,m}(s) + (\hat{\mathcal{Q}}_n^- + \mathcal{Q}_n^+ \tilde{\mathcal{S}}^+_n(s))\tilde{\mathcal{G}}_{n,m}(s) = \mathcal{O}$$

$$[\mathcal{Q}_n^- \tilde{\mathcal{S}}^-_n(s) + \hat{\mathcal{Q}}_n]\tilde{\mathcal{G}}_{n,m}(s) + \mathcal{Q}_n^+ \tilde{\mathcal{G}}_{n+1,m}(s) = \mathcal{O},$$

where $\mathcal{O}$ is the zero matrix. This leads to the relation

$$\tilde{\mathcal{S}}^{\pm}_n(s) = [s\mathcal{I} - \mathcal{Q}_{n\pm1} - \mathcal{Q}^{\pm}_{n\pm1}\tilde{\mathcal{S}}^{\pm}_{n\pm1}(s)]^{-1}\mathcal{Q}^{\mp}_{n\pm1} \tag{E11}$$

that allows expressing $\tilde{\mathcal{S}}^+_n(s)$ in terms of all matrices with higher n and $\tilde{\mathcal{S}}^-_n(s)$ in terms of all matrices with lower n.

For $m = n$ Eq. (E9) reads

$$[\mathcal{Q}_m^- \tilde{\mathcal{S}}^-_m(s) + \hat{\mathcal{Q}}_m + \mathcal{Q}_m^+ \tilde{\mathcal{S}}^+_m(s)]\tilde{\mathcal{G}}_{m,m}(s) = -\mathcal{I}. \tag{E12}$$

The Green's function matrices can now be written as

$$\tilde{\mathcal{G}}_{m,m}(s) = [\mathcal{Q}_m^- \tilde{\mathcal{S}}^-_m - \hat{\mathcal{Q}}_m - \mathcal{Q}_m^- \tilde{\mathcal{S}}^+_m(s)]^{-1}. \tag{E13}$$

For $m = 0$ this becomes

$$\tilde{\mathcal{G}}_{0,0}(s) = [\hat{\mathcal{Q}}_m - \mathcal{Q}_m^- \tilde{\mathcal{S}}^+_m(s)]^{-1}, \tag{E14}$$

which can be expressed as the continued fraction

$$\tilde{\mathcal{G}}_{0,0}(s) = \cfrac{\mathcal{I}}{s\mathcal{I} - \mathcal{Q}_0 - \mathcal{Q}_0^+ \cfrac{\mathcal{I}}{s\mathcal{I} - \mathcal{Q}_1 - \mathcal{Q}_1^+ \cfrac{\mathcal{I}}{s\mathcal{I} - \mathcal{Q}_2 - \cdots}\mathcal{Q}_2^-}\mathcal{Q}_1^-}. \tag{E15}$$

The remaining Green's functions matrices $\tilde{\mathcal{G}}_{0,0}(s)$ can be found in a similar way. The Green's function matrices with $n \neq m$ can be found by multiplying with $\tilde{\mathcal{S}}^+_{n-1}(s)\tilde{\mathcal{S}}^+_{n-2}(s)\cdots\tilde{\mathcal{S}}^+_m(s)$ or $\tilde{\mathcal{S}}^-_{n+1}(s)\tilde{\mathcal{S}}^-_{n+2}(s)\cdots\tilde{\mathcal{S}}^-_m(s)$.

The full Green's function $\tilde{\mathcal{G}}(s)$ can be calculated using Eq. (E11) to find the connection matrices $\tilde{\mathcal{S}}^{\pm}$. Using that $\tilde{\mathcal{S}}^-_0$ is zero and truncating the recurrence relation for $\tilde{\mathcal{S}}^+$ at some level n by setting $\tilde{\mathcal{S}}^+_n$ equal to zero, any matrix element $\tilde{\mathcal{G}}(s)_{mm}$ are then be obtained using Eq. (E13). All other matrix elements $\tilde{\mathcal{G}}(s)_{nm}$ are obtained from Eq. (E10).

[1] T. Creighton, *Proteins: Structures and Molecular Properties* (Freeman, New York, 1993).
[2] T. Kühn and H. Schwalbe, J. Am. Chem. Soc. **122**, 6169 (2000).
[3] M. Pfuhl and P. C. Driscoll, Philos. Trans. R. Soc. London, Ser. A **358**, 513 (2000).
[4] J. Balbach, J. Am. Chem. Soc. **122**, 5887 (2000).
[5] X. G. Chen, P. S. Li, J. S. W. Holtz, Z. H. Chi, V. Pajcini, S. A. Asher, and L. A. Kelly, J. Am. Chem. Soc. **118**, 9705 (1996).
[6] E. T. Spiro, *Biological Applications of Raman Spectroscopy* (Wiley-Interscience, New York, 1987), Vol. 1.
[7] D. J. Segel, A. Bachmann, J. Hofrichter, K. O. Hodgson, S. Doniach, and T. Kiefhaber, J. Mol. Biol. **288**, 489 (1999).
[8] S. Arai and M. Hirai, Biophys. J. **76**, 2192 (1999).
[9] B. Perman, S. Anderson, M. Schmidt, and K. Moffat, Cell. Mol. Biol. (Paris) **46**, 895 (2000).
[10] T. Hori, H. Moriyama, J. Kawaguchi, Y. Hayashi-Iwasaki, T. Oshima, and N. Tanaka, Protein Eng. **13**, 527 (2000).
[11] H. Torii and M. Tasumi, J. Chem. Phys. **96**, 3379 (1992).
[12] H. Torii and M. Tasumi, *Infrared Spectroscopy of Biomolecules* (Wiley, New York, 1996).
[13] M. Jackson, P. I. Haris, and D. Chapman, J. Mol. Struct. **214**, 329 (1989).
[14] W. K. Surewicz and H. H. Mantsch, Biochim. Biophys. Acta **952**, 115 (1988).
[15] D. M. Byler and H. Susi, Biopolymers **25**, 469 (1986).
[16] Y. Tanimura and S. Mukamel, J. Chem. Phys. **99**, 9496 (1993).
[17] Chem. Phys., Special Issue: Multidimensional Spectroscopy, Vol. 266, No. 2, 3 (2001), edited by S. Mukamel and R. M. Hochstrasser.
[18] R. R. Ernst, G. Bodenhausen, and A. Wokaun, *The International Series of Monographs on Chemistry*, Principles of Nuclear Magnetic Resonance in One and Two Dimensions, Vol. 14 (Clarendon, Oxford, 1987).
[19] K. Wtrich, *NMR of Proteins and Nucleic Acids* (Wiley, New York, 1995).
[20] P. Hamm, M. Lim, W. F. DeGrado, and R. M. Hochstrasser, Proc. Natl. Acad. Sci. U.S.A. **96**, 2036 (1999).
[21] P. Hamm, M. Lim, W. F. DeGrado, and R. M. Hochstrasser, J. Chem. Phys. **112**, 1907 (2000).
[22] M. T. Zanni, S. Gnanakaran, J. Stenger, and R. M. Hochstrasser, J. Phys. Chem. B **105**, 6520 (2001).
[23] R. M. Hochstrasser, Chem. Phys. **266**, 273 (2001).
[24] I. V. Rubtsov and R. M. Hochstrasser, J. Phys. Chem. B **106**, 9165 (2002).
[25] S. Woutersen and P. Hamm, J. Phys. Chem. B **104**, 11316 (2000).
[26] S. Woutersen, Y. Mu, G. Stock, and P. Hamm, Proc. Natl. Acad. Sci. U.S.A. **98**, 11254 (2001).
[27] N. H. Ge, M. T. Zanni, and R. M. Hochstrasser, J. Phys. Chem. A **106**, 962 (2002).
[28] S. Woutersen, R. Pfister, P. Hamm, Y. Mu, D. S. Kosov, and G. Stock, J. Chem. Phys. **117**, 6833 (2002).
[29] S. Woutersen and P. Hamm, J. Chem. Phys. **115**, 7737 (2001).
[30] I. V. Rubtsov, J. P. Wang, and R. M. Hochstrasser, J. Phys. Chem. A **107**, 3384 (2003).
[31] P. Hamm, M. H. Lim, and R. M. Hochstrasser, J. Phys. Chem. B **102**, 6123 (1998).
[32] S. Woutersen and P. Hamm, J. Chem. Phys. **114**, 2727 (2001).
[33] J. Edler, P. Hamm, and A. C. Scott, Phys. Rev. Lett. **88**, 067403 (2002).
[34] C. M. Cheatum, A. Tokmakoff, and J. Knoester, J. Chem. Phys. **120**, 8201 (2004).
[35] S. Mukamel and D. Abramavicius, Chem. Rev. (Washington, D.C.) **104**, 2073 (2004).
[36] V. Chernyak, W. M. Zhang, and S. Mukamel, J. Chem. Phys. **109**, 9587 (1998).

[37] S. Mukamel, Phys. Rev. A **28**, 3480 (1983).
[38] R. Kubo, J. Math. Phys. **4**, 174 (1963).
[39] R. Kubo, in *Stochastic Processes in Chemical Physics*, Advances in Chemical Physics Vol. XV, edited by K. E. Shuler (Wiley, New York, 1969), p. 101.
[40] J. H. Freed, G. V. Bruno, and C. F. Polnaszek, J. Phys. Chem. **75**, 3385 (1971).
[41] D. J. Schneider and J. H. Freed, in *Lasers, Molecules, and Methods*, Advances in Chemical Physics Vol. LXXIII, edited by J. O. Hirschfelder, R. E. Wyatt, and R. D. Coalson (Wiley, New York, 1989), p. 387.
[42] D. Gamliel and H. Levanon, *Stochastic Processes in Magnetic Resonance* (World Scientific, River Edge, NJ, 1995).
[43] R. A. MacPhail, R. G. Snyder, and H. L. Strauss, J. Chem. Phys. **77**, 1118 (1982).
[44] J. J. Turner, C. M. Gordon, and S. M. Howdle, J. Phys. Chem. **99**, 17532 (1995).
[45] J. Jeener, B. H. Meier, P. Bachmann, and R. R. Ernst, J. Chem. Phys. **71**, 4546 (1979).
[46] R. Kubo, in *Fluctuation, Relaxation and Resonance in Magnetic Systems*, edited by D. ter Haar (Oliver & Boyd, Edinbourgh, 1962), p. 23.
[47] S. Zamir, R. Poupko, Z. Luz, and S. Alexander, J. Chem. Phys. **94**, 5939 (1991).
[48] A. G. Redfield, Adv. Magn. Reson. **1**, 1 (1965).
[49] Y. Tanimura and S. Mukamel, J. Phys. Soc. Jpn. **63**, 66 (1994).
[50] V. Chernyak and S. Mukamel, J. Chem. Phys. **105**, 4565 (1996).
[51] H. Risken, *The Fokker-Planck Equation* (Springer, Berlin, 1984).
[52] S. Mukamel, *Principles of Nonlinear Optical Spectroscopy* (Oxford University Press, New York, 1995).
[53] C. P. Lawrence and J. L. Skinner, J. Chem. Phys. **117**, 5827 (2002).
[54] C. P. Lawrence and J. L. Skinner, J. Chem. Phys. **117**, 8847 (2002).
[55] R. Rey, K. B. Møller, and J. T. Hynes, Chem. Rev. (Washington, D.C.) **104**, 1915 (2004).
[56] R. Rey and J. T. Hynes, J. Chem. Phys. **104**, 2356 (1996).
[57] K. Kwac and M. H. Cho, J. Chem. Phys. **119**, 2247 (2003).
[58] K. Kwac and M. H. Cho, J. Chem. Phys. **119**, 2256 (2003).
[59] K. Kwac, H. Lee, and M. Cho, J. Chem. Phys. **120**, 1477 (2004).
[60] R. Schweitzer-Stenner, F. Eker, Q. Huang, and K. Griebenow, J. Am. Chem. Soc. **123**, 9628 (2001).
[61] Y. Mu, D. S. Kosov, and G. Stock, J. Phys. Chem. B **107**, 5064 (2003).
[62] R. Schweitzer-Stenner, Biophys. J. **83**, 523 (2002).
[63] P. Bour and T. A. Keiderling, J. Chem. Phys. **119**, 11253 (2003).
[64] H. Torii and M. Tasumi, J. Raman Spectrosc. **29**, 81 (1998).
[65] A. M. Moran, S. M. Park, J. Dreyer, and S. Mukamel, J. Chem. Phys. **118**, 3651 (2003).
[66] R. Venkatramani, T. l. C. Jansen, J. Dreyer, and S. Mukamel, *TRVS XI Conference Proceedings*, 2003.
[67] R. Venkatramani and S. Mukamel, J. Chem. Phys. **117**, 11089 (2002).
[68] A. Piryatinski, V. Chernyak, and S. Mukamel, Chem. Phys. **266**, 285 (2001).
[69] A. Piryatinski, V. Chernyak, and S. Mukamel, Chem. Phys. **266**, 311 (2001).
[70] S. Gnanakaran and A. E. Garcia, J. Phys. Chem. B **107**, 12555 (2003).
[71] A. E. Garcia, Polymer **45**, 669 (2004).
[72] F. Mohamadi, N. G. J. Richards, W. C. Guida *et al.*, J. Comput. Chem. **11**, 440 (1990).
[73] G. M. Crippen and T. F. Havel, J. Chem. Inf. Comput. Sci. **30**, 222 (1990).
[74] U. Essmann, L. Perera, M. L. Berkowitz, T. Darden, H. Lee, and L. G. Pedersen, J. Chem. Phys. **103**, 8577 (1995).
[75] B. R. Brooks, R. E. Bruccoleri, B. D. Olafson, D. J. States, S. Swaminathan, and M. Karplus, J. Comput. Chem. **4**, 187 (1983).
[76] J. Tirado-Rrives and W. L. Jorgensen, Biochem. J. **30**, 3864 (1991).
[77] H. C. Andersen, J. Chem. Phys. **72**, 2384 (1980).
[78] S. Nose and M. L. Klein, Mol. Phys. **50**, 1055 (1983).
[79] W. G. Hoover, Phys. Rev. A **31**, 1695 (1985).
[80] H. Hu, M. Elstner, and J. Hermans, Proteins: Struct., Funct., Genet. **50**, 451 (2003).
[81] M. H. Zaman, M.-Y. Shen, R. S. Berry, K. F. Freed, and T. R. Sosnick, J. Mol. Biol. **331**, 693 (2003).
[82] C. Scheurer, A. Piryatinski, and S. Mukamel, J. Am. Chem. Soc. **123**, 3114 (2001).
[83] S. Krimm and J. Bandekar, Adv. Protein Chem. **38**, 181 (1986).
[84] W. H. Press, S. A. Teukolsky, W. T. Vetterling, and B. P. Flannery, *Numerical Recipes in C*, 2nd ed. (Cambridge University Press, Cambridge, 1992).
[85] S. Mukamel, Annu. Rev. Phys. Chem. **51**, 691 (2000).
[86] A. Tokmakoff, J. Chem. Phys. **105**, 1 (1996).